General Disclaimer

One or more of the Following Statements may affect this Document

- This document has been reproduced from the best copy furnished by the organizational source. It is being released in the interest of making available as much information as possible.

- This document may contain data, which exceeds the sheet parameters. It was furnished in this condition by the organizational source and is the best copy available.

- This document may contain tone-on-tone or color graphs, charts and/or pictures, which have been reproduced in black and white.

- This document is paginated as submitted by the original source.

- Portions of this document are not fully legible due to the historical nature of some of the material. However, it is the best reproduction available from the original submission.

Dynamical and Photometric Investigation of Cometary Type II Tails

GRANT NGR 09-015-159

Semiannual Progress Report No. 8

For the period March 15 to September 14, 1975

Principal Investigator

Dr. Zdenek Sekanina

Prepared for

National Aeronautics and Space Administration

Washington, D.C. 20546

Smithsonian Institution
Astrophysical Observatory
Cambridge, Massachusetts 02138

Dynamical and Photometric Investigation of Cometary Type II Tails

GRANT NGR 09-015-159

Semiannual Progress Report No. 8

For the period March 15 to September 14, 1975

Principal Investigator

Dr. Zdenek Sekanina

Prepared for

National Aeronautics and Space Administration
Washington, D.C. 20546

Smithsonian Institution
Astrophysical Observatory
Cambridge, Massachusetts 02138

TABLE OF CONTENTS

ABSTRACT

The absolute calibration of the photometric profile of the antitail of Comet Kohoutek 1973 XII on plates taken with the Curtis Schmidt telescope of the University of Michigan at the Cerro Tololo Inter-American Observatory is described in detail. The formula for the determination of the air mass, and the corrections for atmospheric absorption and for the loss of light due to vignetting are included. The calibration stars are then used to derive the coefficients converting the relative intensity scale to the absolute surface-brightness units.

The extensive results of the study of the orbital evolution of vaporizing dust particles are listed in a tabular form. Gradual evaporation from the surface of a particle results typically in its expulsion from the solar system. The properties of the particle and the elements of its orbit at expulsion are given as functions of the particle's properties and orbit before appreciable evaporation commenced. Also given are circumstances at an encounter of an expelled particle with the earth as a function of the particle's properties. A few specific cases are represented graphically.

Other activities during the half year are briefly reported, such as a progress in the statistical analysis of the occurrences of anomalous tails of comets and their prediction, a study of the band structures in the dust tails of some comets, etc.

Listed as addenda are two papers presented at the IAU Colloquium No. 31 "Interplanetary Dust and Zodiacal Light" held in June 1975, and a review on the dust tails prepared for the triennial report of the IAU Commission 15 (The Physical Study of Comets, Minor Planets and Meteorites).

PART A. ABSOLUTE CALIBRATION OF THE CERRO TOLOLO PLATES OF COMET KOHOUTEK (1973 XII ≡ 1973f)

I. Calibration stars

The Semiannual Progress Report No. 6 (for the period March 15 to September 14, 1974) presented the results of the photometric study of the antitail of Comet Kohoutek from the plates taken under the supervision of Dr. F. D. Miller, University of Michigan, at the Cerro Tololo Inter-American Observatory in Chile. The analysis of the plates was then completed as far as relative photometry was concerned, but nothing was done to reduce the data to an absolute photometric system, because the magnitudes of the calibration stars were unknown.

Courtesy of Professor W. Liller, Center for Astrophysics, I acquired the missing information earlier this year and the paper on the antitail of Comet Kohoutek was subsequently completed and submitted for publication (Sekanina and Miller 1975). The calibration procedure is briefly described in the paper, but for the sake of conciseness all intermediate steps were omitted. It is the purpose of this part of the report to give more details on the calibration stars and the absolute photometric reduction of the plates.

Table I gives for each calibration star the red magnitude outside the earth's atmosphere $R_*(0)$ as derived by Liller; the relative brightness of the sky background I_S on the star's profile tracing (which is not identical with the sky brightness at the star's position on the antitail radial tracings); the star's peak relative brightness I_*; the star's width factor σ; the star's trail length L; and the red-magnitude difference between the surface brightness

Table I. Calibration stars

Calibration star	Plate	$R_*(0)$	I_S	I_*	σ	L	R_S-R_*
A	15520	$13^m.34$	104.9	54.6	$2''.48$	$157''.0$	$6^m.76$
B	15520	13.04	103.5	60.8	2.93	157.9	7.08
C	15554	12.95	100.4	63.8	2.13	242.1	7.29
D	15554	13.49	99.2	29.4	2.36	240.9	6.56
E	15687	13.29	106.0	30.3	3.31	161.6	6.46
F	15687	13.12	107.4	42.9	2.44	165.8	6.52
G	15703	13.93	106.3	18.7	3.01	146.1	5.72
H	15703	14.54	106.3	11.3	3.16	137.2	5.16
J	15703	13.69	105.4	27.8	3.08	152.2	6.23

of 1 square arcsec of the sky at the star's position and the star's brightness $R_S - R_*$. Some of the data in Table I are the revised figures of Table IV of Semiannual Report No. 6.

II. Air mass determination, correction for atmospheric absorption, and the vignetting effect

Since the observations were made at very low altitudes, atmospheric absorption was severe even in the red light, and its effects had to be reduced carefully. The air mass X at Cerro Tololo was calculated as a function of zenith distance following a formula by Crawford and Landolt (1965):

$$X = \sec z - \Delta X \ , \tag{1}$$

where z is the zenith distance and ΔX is a correction given by

$$\Delta X = 0.0018167\ \zeta + 0.002875\ \zeta^2 + 0.0008083\ \zeta^3 \ , \tag{2}$$

where

$$\zeta = \sec z - 1 \ . \tag{3}$$

The red magnitude outside the earth's atmosphere R_0 is then related to the red magnitude R_X at air mass X by

$$R_0 = R_X - k_R X \ , \tag{4}$$

where k_R is the absorption coefficient, whose value at Cerro Tololo amounts, on an average, to $0^m.07$ per air mass (Liller, personal communication).

Further, the photometric tracings were corrected for a light-loss effect due to geometrical vignetting of the Curtis Schmidt camera. On the 20 cm-by-20 cm plates the vignetting effect is negligible at distances smaller than about

3 to 4 cm from the plate center. The Cassegrain hole starts vignetting at a 2.5-cm distance from the center at a rate of about $0^m.006$ per radial cm, the primary starts vignetting at a 7.5-cm distance; at a distance of 9 cm from the center the effect is $0^m.07$ and the loss of light increases at a rate of $0^m.05$ per radial cm afterwards (Miller, personal communication).

III. The results

The relative intensities of the antitail on each plate were expressed in arbitrary units, related to a particular photographic density on the plate. The absolute calibration required to find the conversion factor between the relative-intensity scale and the absolute surface-brightness units for the observed air masses and the implied vignetting effect, and then to extrapolate the antitail's brightness to outside the earth's atmosphere.

Table II lists the basic steps in the calculation of the sky brightness. For each calibration star the table gives the effective zenith distance; the correction ΔX from (2); the air mass X from (1); the magnitude correction for the air mass X, $R_*(X) - R_*(0)$; the vignetting effect; the star's R magnitude at the given air mass and including the vignetting correction, $R_*(X, \text{vign.})$; the R magnitude of 1 square arcsec of the sky at the star's position on the radial tracings of the antitail, $R_S(J_S)$; the surface brightness of the sky in the red S_{10} units (the equivalent number of magnitude 10 stars per square degree); the relative intensity of the sky at the star's position J_S; and the surface brightness S_{10} corresponding to 100 units of the relative brightness scale.

Table III lists for each plate an averaged value of S_{10} (from the last column of Table II) and an estimated relative error; the zenith distance of

Table II. Observed surface brightness of the sky background

Calibration star	Zenith distance*)	ΔX	X	$R_*(X)-R_*(0)$	Vignetting	$R_*(X,\text{vign.})$	$R_S(J_S)$	$S_{10}(J_S)$	J_S	$S_{10}(100)$
	°			m	m	m	m			
A	76.1	0.06	4.10	0.29	0.02	13.65	20.41	888	101.4	876
B	75.7	0.05	3.99	0.28	0.01	13.33	20.41	888	98.5	902
C	78.6	0.11	4.95	0.35	.	13.30	20.59	753	105.5	714
D	78.5	0.11	4.91	0.34	.	13.83	20.39	905	101.9	888
E	74.0	0.04	3.59	0.25	.	13.54	20.00	1296	101.2	1281
F	73.6	0.04	3.51	0.25	.	13.37	19.89	1434	102.9	1394
G	74.1	0.04	3.61	0.25	.	14.18	19.90	1421	102.1	1392
H	74.1	0.04	3.61	0.25	.	14.79	19.95	1357	102.1	1329
J	74.0	0.04	3.59	0.25	.	13.94	20.17	1108	101.9	1087

*) At midexposure; free from refraction.

Table III. Absolute calibration of the antitail

Plate	$\bar{S}_{10}(100)$	Relative m.e.	Zenith distance*)	ΔX	X	Vignetting	$R_*(X,\text{vign.}) - R_*(0)$	$S_{10}(100,\infty)$
15520	889	± 2%	76°.6	0.07	4.25	$0^m.03$ to $0^m.05$	$0^m.33$ to $0^m.35$	1205 to 1227
15554	801	±15	78.3	0.10	4.83	.	$0^m.34$	1095
15687	1337	± 6	73.9	0.04	3.57	.	0.25	1683
15703	1269	±13	74.0	0.04	3.59	.	0.25	1598

*) In the middle of the antitail at mid-exposure; free from refraction

the middle of the antitail; the correction ΔX from (2); the air mass X from (1); the difference between the observed magnitude and the magnitude extrapolated outside the earth's atmosphere R(X,vign.) - R(0); and the surface brightness in S_{10} units corresponding to 100 units on the relative scale and extrapolated outside the earth's atmosphere, $S_{10}(100,\infty)$. Significant differential effects were found only on plate No. 15520, where the comet was placed well off the center, apparently in the expectation of a long regular tail. Since such a tail did not materialize, the comet was positioned near the plate center on the subsequent photographs, on which the vignetting effect was negligible. The differential effect of the air mass was never important, as can be seen from a comparison of Tables II and III for plates 15554, 15687 and 15703.

IV. References

Crawford, D. L., and Landolt, A. U. (1965). Tables for use at the Cerro Tololo Inter-American Observatory. Contr. Cerro Tololo Inter-Amer. Obs. No. 7.

Sekanina, Z., and Miller, F. D. (1975). On the nature of the anti-tail of Comet Kohoutek (1973f). II. Comparison of the working model with ground-based photographic observations. Center for Astrophys. Preprint Series No. 312. Submitted to Icarus.

PART B. ORBITAL EVOLUTION OF VAPORIZING DUST PARTICLES

I. Introduction

Part A of the Semiannual Report No. 7 (for the period September 15, 1974 to March 14, 1975) described the method that solves the equations of motion under a central attraction, whose strength gradually declines with time. This method was applied to determine the evolution of orbits of vaporizing dust particles. A study of Comet Kohoutek 1973 XII (Sekanina and Miller 1975) suggested that the large particles in the antitail were probably subject to appreciable evaporation near the sun. It was felt that an investigation of the orbital evolution of vaporizing dust particles was essential for a better understanding of the properties of dust in cometary tails. The basic results of such an investigation were presented at the IAU Colloquium No. 31 "Interplanetary Dust and Zodiacal Light", held at Heidelberg, Germany, last June (see Addendum I). The details of the calculations, not included in the Heidelberg paper, are summarized in the next two sections.

II. The initial conditions

A practical problem that had to be settled was to establish realistic initial dynamical conditions to begin with. Varied in the 64 performed runs were the particle's radius a, its density ρ, its vaporization constants [see formula (9) below], the scattering efficiency for radiation pressure Q_{rp}, and the initial orbital eccentricity e_o. The particle's properties impose a lower limit on its orbit dimensions, because the particle cannot approach

the sun to a distance where the repulsive dynamical effect associated with the increasing rate of evaporation from its surface exceeds substantially the inward spiraling rate caused by the Poynting-Robertson effect (assisted by a pseudo Poynting-Robertson effect from the sputtering). A realistic initial heliocentric distance is still much larger than this critical heliocentric distance, and can conveniently be defined as a distance where the Poynting-Robertson spiraling is dominant. To establish such a distance numerically, we compare the rates of spiraling, in a circular orbit, due to the Poynting-Robertson effect and due to particle evaporation, respectively.

The Poynting-Robertson drag implies a rate (see Semiannual Report No. 7):

$$(dr/dt)_{PR} = -3.42\times10^{-6}(1-\mu)/r \text{ (AU per day)}, \tag{5}$$

where $1-\mu$ is the ratio of radiation pressure to solar gravity and r is the heliocentric distance in AU. Substituting from the formula

$$1-\mu = CQ_{rp}/\rho a \tag{6}$$

where $C = 5.85\times10^{-5}$ g cm^{-2}, ρ is in g cm^{-3} and a in cm, we find

$$(dr/dt)_{PR} = -3.42\times10^{-6}CQ_{rp}/r\rho a \text{ (AU per day)}. \tag{7}$$

If the effect from sputtering is added, we obtain finally

$$(dr/dt)_{PR+s} = -3.42\times10^{-6}C(Q_{rp}+0.25)/r\rho a \text{ (AU per day)}. \tag{8}$$

To derive the rate of spiraling from the particle evaporation, we adopt the following law for the linear vaporization rate of the particle (see pp. I-1 and I-2 of Addendum I):

$$\dot{a} = -(A/\rho)\exp[B(1-r^{\frac{1}{2}})] \text{ (cm/sec)}, \tag{9}$$

where A is the normalized (to 1 AU from the sun) vaporization flux from the particle in g cm^{-2} sec^{-1}, and

$$B = 1.81\ L\ (\varepsilon/\kappa)^{\frac{1}{4}}, \tag{10}$$

L is the latent heat of vaporization in kcal $mole^{-1}$, κ is the absorptivity of the particle's surface for solar radiation and ε its emissivity for re-radiation. The rate of spiraling can now be written thus

$$(dr/dt)_{vap} = [dr/d(1-\mu)] \cdot [d(1-\mu)/da] \cdot \dot{a}\ . \tag{11}$$

The first term on the right-hand side can be derived from Kepler's second law, which requires that

$$\mu q(1+e) = \text{const.}, \tag{12}$$

where q is the perihelion distance and e the eccentricity. In a circular orbit condition (12) is simply

$$\mu r = \text{const.}, \tag{13}$$

so that

$$dr/d(1-\mu) = r/\mu = r(1-CQ_{rp}/\rho a)^{-1}. \tag{14}$$

The second and third terms on the right-hand side of (11) come directly from (6) and (9), respectively, so that (11) can finally be written as:

$$(dr/dt)_{vap} = 8.64\times10^{4}ACQ_{rp}r\ \exp[B(1-r^{\frac{1}{2}})]/\rho a(\rho a-CQ_{rp}). \tag{15}$$

Defining now the ratio

$$|(dr/dt)_{vap}|/|(dr/dt)_{PR+s}| = \xi\ , \tag{16}$$

we can determine an initial heliocentric distance r_o when keeping $\xi << 1$. The solution can be formulated as a transcendental equation

$$Br_o^{\frac{1}{2}} = \log_e(Wr_o^2) \ , \tag{17}$$

where

$$W = 2.53\times10^{10}Ae^{BQ_{rp}}/\xi(Q_{rp}+0.25)(\rho a-CQ_{rp}) \ . \tag{18}$$

The initial heliocentric distances calculated from (17) for $\xi = 0.1$ are listed in Table IV.

III. The numerical results

The basic conclusions of the study are summarized in Addendum I. Here I present a series of tables that illustrate the conclusions numerically.

Tables V to VII list the final $1-\mu$ value of the particle, i.e., at the time of expulsion from the solar system. Table V gives it, as a function of the particle's vaporization constants, the density and the scattering efficiency, for an initial particle radius of 1 micron and a zero initial orbital eccentricity. Table VI gives it, as a function of the initial particle size, the normalized vaporization flux, the density and the scattering efficiency, for a latent vaporization heat equivalent to $B = 150$ and a zero initial orbital eccentricity. And Table VII gives it, as a function of the initial orbital eccentricity, the normalized vaporization flux, the density and the scattering efficiency, for an initial particle radius of 1 micron and a latent vaporization heat equivalent to $B = 150$.

Tables VIII to X arrange in the same way the final particle radius (in microns); Tables XI to XIII the perihelion distance of the final orbit (in AU);

Table IV. Initial heliocentric distances (AU)

B	ρ (g cm^{-3})	Q_{rp}	Initial particle radius					
			1 micron		5 microns		10 microns	
			$Ae^B = 10^6$	$Ae^B = 10^8$	$Ae^B = 10^6$	$Ae^B = 10^8$	$Ae^B = 10^6$	$Ae^B = 10^8$
50	2	1.0	0.944	1.149	0.866	1.063	0.837	1.031
		1.5	0.957	1.162	0.870	1.067	0.840	1.034
	4	1.0	0.908	1.108	0.837	1.031	0.809	1.000
		1.5	0.914	1.115	0.840	1.034	0.812	1.003
100	2	1.0	0.208	0.256	0.189	0.236	0.182	0.228
		1.5	0.210	0.259	0.190	0.237	0.183	0.229
	4	1.0	0.199	0.246	0.182	0.228	0.176	0.221
		1.5	0.200	0.248	0.183	0.229	0.176	0.221
150	4	1.0	0.0815	0.102	0.0743	0.0939	0.0715	0.0908
		2.0	0.0827	0.103	0.0749	0.0945	0.0720	0.0913
	8	1.0	0.0782	0.0983	0.0715	0.0908	0.0687	0.0877
		2.0	0.0790	0.0991	0.0720	0.0913	0.0692	0.0882
200	4	1.0	0.0431	0.0543	0.0392	0.0500	0.0377	0.0482
		2.0	0.0438	0.0550	0.0395	0.0503	0.0380	0.0485
	8	1.0	0.0414	0.0523	0.0377	0.0482	0.0362	0.0466
		2.0	0.0418	0.0528	0.0380	0.0485	0.0364	0.0468

Table V. The final 1-μ for a = 1 micron and e_o = 0

B	Ae^B	Particle density						
		2 g cm^{-3}		4 g cm^{-3}			8 g cm^{-3}	
		Q_{rp} = 1.0	Q_{rp} = 1.5	Q_{rp} = 1.0	Q_{rp} = 1.5	Q_{rp} = 2.0	Q_{rp} = 1.0	Q_{rp} = 2.0
50	10^6	0.835	0.864	0.810	0.823	.	.	.
	10^8	0.824	0.856	0.802	0.815	.	.	.
100	10^6	0.835	0.864	0.813	0.827	.	.	.
	10^8	0.820	0.852	0.798	0.811	.	.	.
150	10^6	.	.	0.812	.	0.839	0.803	0.819
	10^8	.	.	0.799	.	0.824	0.788	0.799
200	10^6	.	.	0.808	.	0.840	0.806	0.817
	10^8	.	.	0.793	.	0.822	0.783	0.803

Table VI. The final 1-μ for B = 150 and e_o = 0

Initial particle radius a (micron)	Ae^B	Particle density			
		4 g cm^{-3}		8 g cm^{-3}	
		Q_{rp} = 1.0	Q_{rp} = 2.0	Q_{rp} = 1.0	Q_{rp} = 2.0
1	10^6	0.812	0.839	0.803	0.819
	10^8	0.799	0.824	0.788	0.799
5	10^6	0.801	0.809	0.806	0.806
	10^8	0.790	0.791	0.780	0.786
10	10^6	0.806	0.806	0.790	0.815
	10^8	0.780	0.786	0.782	0.799

Table VII. The final 1-μ for a = 1 micron and B = 150

Initial orbital eccentricity e_o	Ae^B	Particle density			
		4 g cm^{-3}		8 g cm^{-3}	
		Q_{rp} = 1.0	Q_{rp} = 2.0	Q_{rp} = 1.0	Q_{rp} = 2.0
0.0	10^6	0.812	0.839	0.803	0.819
	10^8	0.799	0.824	0.788	0.799
0.1	10^6	0.597	0.671	0.558	0.601
	10^8	0.592	0.660	0.560	0.591
0.2	10^6	0.562	0.642	0.518	0.561
	10^8	0.550	0.635	0.509	0.555

Table VIII. The final particle radius (micron) for a = 1 micron and $e_o = 0$

B	Ae^B	Particle density						
		2 g cm^{-3}		4 g cm^{-3}			8 g cm^{-3}	
		$Q_{rp} = 1.0$	$Q_{rp} = 1.5$	$Q_{rp} = 1.0$	$Q_{rp} = 1.5$	$Q_{rp} = 2.0$	$Q_{rp} = 1.0$	$Q_{rp} = 2.0$
50	10^6	0.344	0.499	0.177	0.262	.	.	.
	10^8	0.348	0.503	0.179	0.264	.	.	.
100	10^6	0.344	0.498	0.176	0.260	.	.	.
	10^8	0.350	0.505	0.180	0.266	.	.	.
150	10^6	.	.	0.177	.	0.342	0.089	0.175
	10^8	.	.	0.180	.	0.348	0.091	0.180
200	10^6	.	.	0.178	.	0.342	0.089	0.176
	10^8	.	.	0.181	.	0.349	0.092	0.179

Table IX. The final particle radius (micron) for B = 150 and $e_o = 0$

Initial particle radius a (micron)	Ae^B	Particle density			
		4 g cm^{-3}		8 g cm^{-3}	
		$Q_{rp} = 1.0$	$Q_{rp} = 2.0$	$Q_{rp} = 1.0$	$Q_{rp} = 2.0$
1	10^6	0.177	0.342	0.089	0.175
	10^8	0.180	0.348	0.091	0.180
5	10^6	0.179	0.355	0.089	0.178
	10^8	0.182	0.363	0.092	0.183
10	10^6	0.178	0.356	0.091	0.176
	10^8	0.184	0.365	0.092	0.180

Table X. The final particle radius (micron) for a = 1 micron and B = 150

Initial orbital eccentricity e_o	Ae^B	Particle density			
		4 g cm^{-3}		8 g cm^{-3}	
		$Q_{rp} = 1.0$	$Q_{rp} = 2.0$	$Q_{rp} = 1.0$	$Q_{rp} = 2.0$
0.0	10^6	0.177	0.342	0.089	0.175
	10^8	0.180	0.348	0.091	0.180
0.1	10^6	0.241	0.427	0.129	0.239
	10^8	0.242	0.435	0.128	0.243
0.2	10^6	0.255	0.447	0.139	0.256
	10^8	0.261	0.452	0.141	0.258

Table XI. The final perihelion distance (AU) for a = 1 micron and $e_o = 0$

B	Ae^B	Particle density						
		2 g cm^{-3}		4 g cm^{-3}			8 g cm^{-3}	
		$Q_{rp} = 1.0$	$Q_{rp} = 1.5$	$Q_{rp} = 1.0$	$Q_{rp} = 1.5$	$Q_{rp} = 2.0$	$Q_{rp} = 1.0$	$Q_{rp} = 2.0$
50	10^6	0.772	0.772	0.759	0.754	.	.	.
	10^8	0.952	0.950	0.937	0.932	.	.	.
100	10^6	0.169	0.169	0.167	0.165	.	.	.
	10^8	0.211	0.210	0.209	0.207	.	.	.
150	10^6	.	.	0.0684	.	0.0670	0.0681	0.0664
	10^8	.	.	0.0860	.	0.0846	0.0857	0.0837
200	10^6	.	.	0.0361	.	0.0353	0.0360	0.0350
	10^8	.	.	0.0458	.	0.0449	0.0456	0.0444

Table XII. The final perihelion distance (AU) for B = 150 and $e_o = 0$

Initial particle radius a (micron)	Ae^B	Particle density			
		4 g cm^{-3}		8 g cm^{-3}	
		$Q_{rp} = 1.0$	$Q_{rp} = 2.0$	$Q_{rp} = 1.0$	$Q_{rp} = 2.0$
1	10^6	0.0684	0.0670	0.0681	0.0664
	10^8	0.0860	0.0846	0.0857	0.0837
5	10^6	0.0679	0.0659	0.0682	0.0657
	10^8	0.0852	0.0833	0.0850	0.0829
10	10^6	0.0682	0.0657	0.0678	0.0656
	10^8	0.0850	0.0829	0.0845	0.0834

Table XIII. The final perihelion distance (AU) for a = 1 micron and B = 150

Initial orbital eccentricity e_o	Ae^B	Particle density			
		4 g cm^{-3}		8 g cm^{-3}	
		$Q_{rp} = 1.0$	$Q_{rp} = 2.0$	$Q_{rp} = 1.0$	$Q_{rp} = 2.0$
0.0	10^6	0.0684	0.0670	0.0681	0.0664
	10^8	0.0860	0.0846	0.0857	0.0837
0.1	10^6	0.0640	0.0636	0.0629	0.0619
	10^8	0.0815	0.0810	0.0802	0.0792
0.2	10^6	0.0635	0.0632	0.0623	0.0614
	10^8	0.0810	0.0807	0.0796	0.0787

and Tables XIV to XVI an upper hyperbolic limit, $(1/a)_{max}$, on the reciprocal semimajor axis of the final orbit (in AU^{-1}), the lower limit being defined, of course, by a parabola.

The upper limit $(1/a)_{max}$ can be approximated by assuming that the last time the particle approaches the sun it does so along a parabolic orbit, and that the dynamical effect of evaporation during the last return can be expressed as an abrupt change in $1-\mu$ at perihelion. Then we can write

$$k^2\mu\,[2/q - (1/a)_{max}] = 2k^2\mu_o/a\ ; \qquad (19)$$

where k is the gravitation constant, q the perihelion distance, and μ_o and μ refer to the parabolic and the final orbits, respectively. Writing $\Delta(1-\mu) = \mu_o-\mu$, we have (19) in the form

$$(1/a)_{max} = -2\Delta(1-\mu)/\mu q\ . \qquad (20)$$

Expressing $\Delta(1-\mu)$ through Δa, the loss per revolution in particle radius by evaporation, and using for the latter a formula, applied previously to icy grains of the distant comets (Sekanina 1975) and generalized now to a case when $1-\mu \gg 0$,

$$\Delta a = -1.42\times10^{7}(A/\rho)q^{5/4}(\pi/2B\mu)^{\frac{1}{2}}\exp[B(1-q^{\frac{1}{2}})] \quad \text{(cm/rev.)}, \qquad (21)$$

we find

$$(1/a)_{max} = -6.205\times10^{11}q^{\frac{1}{4}}Q_{rp}(1-\mu)^2\mu^{-3/2}AB^{-\frac{1}{2}}\exp[B(1-q^{\frac{1}{2}})]\ (AU^{-1}). \qquad (22)$$

The remaining quantities of interest are the heliocentric V_H and geocentric V_G velocities of the particle at expulsion for the parabolic and the

Table XIV. The upper hyperbolic limit on the reciprocal semimajor axis (AU^{-1}) of the final orbit for a = 1 micron and e_o = 0

B	Ae^B	Particle density						
		2 g cm^{-3}		4 g cm^{-3}			8 g cm^{-3}	
		Q_{rp} = 1.0	Q_{rp} = 1.5	Q_{rp} = 1.0	Q_{rp} = 1.5	Q_{rp} = 2.0	Q_{rp} = 1.0	Q_{rp} = 2.0
50	10^6	-0.071	-0.068	-0.078	-0.069	.	.	.
	10^8	-0.052	-0.053	-0.061	-0.053	.	.	.
100	10^6	-0.552	-0.580	-0.546	-0.545	.	.	.
	10^8	-0.425	-0.447	-0.416	-0.397	.	.	.
150	10^6	.	.	-1.923	.	-1.929	-1.908	-1.831
	10^8	.	.	-1.530	.	-1.416	-1.482	-1.373
200	10^6	.	.	-4.659	.	-5.026	-4.808	-4.551
	10^8	.	.	-3.495	.	-3.575	-3.482	-3.702

Table XV. The upper hyperbolic limit on the reciprocal semimajor axis (AU^{-1}) of the final orbit for B = 150 and e_o = 0

Initial particle radius a (micron)	Ae^B	Particle density: 4 g cm^{-3}		8 g cm^{-3}	
		Q_{rp} = 1.0	Q_{rp} = 2.0	Q_{rp} = 1.0	Q_{rp} = 2.0
1	10^6	-1.923	-1.929	-1.908	-1.831
	10^8	-1.530	-1.416	-1.482	-1.373
5	10^6	-1.980	-1.903	-1.912	-1.955
	10^8	-1.715	-1.407	-1.640	-1.486
10	10^6	-1.912	-1.955	-1.828	-2.210
	10^8	-1.640	-1.486	-1.899	-1.483

Table XVI. The upper hyperbolic limit on the reciprocal semimajor axis (AU^{-1}) of the final orbit for a = 1 micron and B = 150

Initial orbital eccentricity e_o	Ae^B	Particle density: 4 g cm^{-3}		8 g cm^{-3}	
		Q_{rp} = 1.0	Q_{rp} = 2.0	Q_{rp} = 1.0	Q_{rp} = 2.0
0.0	10^6	-1.923	-1.929	-1.908	-1.831
	10^8	-1.530	-1.416	-1.482	-1.373
0.1	10^6	-1.175	-1.131	-1.234	-1.122
	10^8	-0.920	-0.856	-1.031	-0.833
0.2	10^6	-1.064	-1.026	-1.115	-0.984
	10^8	-0.780	-0.770	-0.846	-0.739

upper hyperbolic limits at 1 AU from the sun; the corresponding limits for the angle of crossing χ (the angle between the vector of the earth's circular velocity V_E and the vector of V_H), counted from the earth's apex away from the sun; and for the intercept angle ϕ (the angle between the vectors of V_E and $-V_G$), counted from the apex toward the sun. The expressions used for calculating the above quantities are as follows:

$$(V_H)_{hyp} = V_E \mu^{\frac{1}{2}} [2-(1/a)_{max}]^{\frac{1}{2}} , \tag{23}$$

$$(V_H)_{par} = V_E (2\mu)^{\frac{1}{2}} , \tag{24}$$

$$(V_G)_{hyp} = V_E \{1 + \mu[2-(1/a)_{max}] - 2(\mu q)^{\frac{1}{2}} [2-q(1/a)_{max}]^{\frac{1}{2}}\}^{\frac{1}{2}} , \tag{25}$$

$$(V_G)_{par} = V_E \{1 + 2\mu^{\frac{1}{2}} [\mu^{\frac{1}{2}} - (2q)^{\frac{1}{2}}]\}^{\frac{1}{2}} , \tag{26}$$

$$\cos \chi = (V_E^2 + V_H^2 - V_G^2)/2V_E V_H , \tag{27}$$

$$\cos \phi = (V_E^2 + V_G^2 - V_H^2)/2V_E V_G , \tag{28}$$

where $V_E = 29.77$ km sec^{-1}. The ranges, from a parabolic limit to the upper hyperbolic limit, of V_H, V_G, χ and ϕ are listed, respectively, in Tables XVII to XIX, XX to XXII, XXIII to XXV and XXVI to XXVIII.

The expulsion lifetimes, counted from the time when $\xi = 0.1$, are presented in Tables XXIX to XXXI. The lifetimes are given only to two significant digits, because their actual values depend rather strongly on the aphelion distances of the last few revolutions before expulsion. All the above tables are organized in the same way as Tables V to VII.

Finally, the results of six of the 64 runs calculated are graphically represented in Figs. 1 to 6. The orbital evolution of each particle begins on

Table XVII. The range of the heliocentric velocities (km sec^{-1}) at expulsion at 1 AU from the sun for a = 1 micron and e_o = 0

B	Ae^B	Particle density						
		2 g cm^{-3}		4 g cm^{-3}			8 g cm^{-3}	
		Q_{rp} = 1.0	Q_{rp} = 1.5	Q_{rp} = 1.0	Q_{rp} = 1.5	Q_{rp} = 2.0	Q_{rp} = 1.0	Q_{rp} = 2.0
50	10^6	17.1 - 17.4	15.5 - 15.8	18.4 - 18.7	17.7 - 18.0	.	.	.
	10^8	17.7 - 17.9	16.0 - 16.2	18.7 - 19.0	18.1 - 18.3	.	.	.
100	10^6	17.1 - 19.3	15.5 - 17.6	18.2 - 20.6	17.5 - 19.8	.	.	.
	10^8	17.9 - 19.7	16.2 - 17.9	18.9 - 20.8	18.3 - 20.0	.	.	.
150	10^6	.	.	18.3 - 25.6	.	16.9 - 23.7	18.7 - 26.1	17.9 - 24.8
	10^8	.	.	18.9 - 25.1	.	17.7 - 23.1	19.4 - 25.6	18.9 - 24.5
200	10^6	.	.	18.4 - 33.7	.	16.8 - 31.6	18.5 - 34.2	18.0 - 32.6
	10^8	.	.	19.2 - 31.7	.	17.8 - 29.7	19.6 - 32.5	18.7 - 31.6

Table XVIII. The range of the heliocentric velocities (km sec^{-1}) at expulsion at 1 AU from the sun for B = 150 and e_o = 0

Initial particle radius a (micron)	Ae^B	Particle density			
		4 g cm^{-3}		8 g cm^{-3}	
		Q_{rp} = 1.0	Q_{rp} = 2.0	Q_{rp} = 1.0	Q_{rp} = 2.0
1	10^6	18.3 - 25.6	16.9 - 23.7	18.7 - 26.1	17.9 - 24.8
	10^8	18.9 - 25.1	17.7 - 23.1	19.4 - 25.6	18.9 - 24.5
5	10^6	18.8 - 26.5	18.4 - 25.7	18.5 - 25.9	18.5 - 26.1
	10^8	19.3 - 26.3	19.2 - 25.1	19.7 - 26.6	19.5 - 25.7
10	10^6	18.5 - 25.9	18.5 - 26.1	19.3 - 26.7	18.1 - 26.3
	10^8	19.7 - 26.6	19.5 - 25.7	19.7 - 27.4	18.9 - 24.9

Table XIX. The range of the heliocentric velocities (km sec^{-1}) at expulsion at 1 AU from the sun for a = 1 micron and B = 150

Initial orbital eccentricity e_o	Ae^B	Particle density			
		4 g cm^{-3}		8 g cm^{-3}	
		Q_{rp} = 1.0	Q_{rp} = 2.0	Q_{rp} = 1.0	Q_{rp} = 2.0
0.0	10^6	18.3 - 25.6	16.9 - 23.7	18.7 - 26.1	17.9 - 24.8
	10^8	18.9 - 25.1	17.7 - 23.1	19.4 - 25.6	18.9 - 24.5
0.1	10^6	26.7 - 33.7	24.1 - 30.2	28.0 - 35.6	26.6 - 33.2
	10^8	26.9 - 32.5	24.5 - 29.3	27.9 - 34.4	26.9 - 32.0
0.2	10^6	27.9 - 34.5	25.2 - 31.0	29.2 - 36.5	27.9 - 34.1
	10^8	28.2 - 33.3	25.4 - 29.9	29.5 - 35.2	28.1 - 32.9

Table XX. The range of the geocentric velocities (km sec^{-1}) at expulsion at 1 AU from the sun for a = 1 micron and e_o = 0

B	Ae^B	Particle density						
		2 g cm^{-3}		4 g cm^{-3}			8 g cm^{-3}	
		Q_{rp} = 1.0	Q_{rp} = 1.5	Q_{rp} = 1.0	Q_{rp} = 1.5	Q_{rp} = 2.0	Q_{rp} = 1.0	Q_{rp} = 2.0
50	10^6	16.9 - 16.8	17.8 - 17.7	16.5 - 16.4	16.9 - 16.8	.	.	.
	10^8	13.1 - 13.0	14.6 - 14.5	12.6 - 12.4	13.2 - 13.0	.	.	.
100	10^6	27.6 - 28.8	27.3 - 28.4	27.8 - 29.2	27.7 - 29.0	.	.	.
	10^8	26.8 - 27.8	26.6 - 27.5	27.0 - 28.2	26.9 - 28.0	.	.	.
150	10^6	.	.	30.6 - 35.3	.	30.2 - 34.3	30.7 - 35.6	30.5 - 34.9
	10^8	.	.	30.2 - 34.3	.	29.9 - 33.2	30.4 - 34.5	30.3 - 34.0
200	10^6	.	.	31.9 - 42.4	.	31.3 - 41.1	31.9 - 42.9	31.8 - 41.7
	10^8	.	.	31.8 - 40.5	.	31.3 - 39.2	32.0 - 41.0	31.6 - 40.5

Table XXI. The range of the geocentric velocities (km sec^{-1}) at expulsion at 1 AU from the sun for B = 150 and $e_o = 0$

Initial particle radius a (micron)	Ae^B	Particle density: 4 g cm^{-3} Q_{rp} = 1.0	4 g cm^{-3} Q_{rp} = 2.0	8 g cm^{-3} Q_{rp} = 1.0	8 g cm^{-3} Q_{rp} = 2.0
1	10^6	30.6 - 35.3	30.2 - 34.3	30.7 - 35.6	30.5 - 34.9
	10^8	30.2 - 34.3	29.9 - 33.2	30.4 - 34.5	30.3 - 34.0
5	10^6	30.8 - 35.9	30.7 - 35.5	30.7 - 35.5	30.8 - 35.7
	10^8	30.4 - 35.1	30.4 - 34.3	30.6 - 35.2	30.5 - 34.7
10	10^6	30.7 - 35.5	30.8 - 35.7	31.0 - 35.9	30.6 - 35.9
	10^8	30.6 - 35.2	30.5 - 34.7	30.5 - 35.9	30.3 - 34.2

Table XXII. The range of the geocentric velocities (km sec^{-1}) at expulsion at 1 AU from the sun for a = 1 micron and B = 150

Initial orbital eccentricity e_o	Ae^B	Particle density: 4 g cm^{-3} Q_{rp} = 1.0	4 g cm^{-3} Q_{rp} = 2.0	8 g cm^{-3} Q_{rp} = 1.0	8 g cm^{-3} Q_{rp} = 2.0
0.0	10^6	30.6 - 35.3	30.2 - 34.2	30.7 - 35.6	30.5 - 34.9
	10^8	30.2 - 34.3	29.9 - 33.2	30.4 - 34.5	30.3 - 34.0
0.1	10^6	34.6 - 40.1	33.3 - 37.8	35.4 - 41.6	34.6 - 39.9
	10^8	33.9 - 38.4	32.8 - 36.4	34.6 - 39.8	34.1 - 38.1
0.2	10^6	35.3 - 40.6	33.8 - 38.3	36.1 - 42.1	35.4 - 40.4
	10^8	34.7 - 38.8	33.2 - 36.7	35.5 - 40.3	34.7 - 38.6

Table XXIII. The range of the angles of crossing (deg) at expulsion at 1 AU from the sun for a = 1 micron and $e_o = 0$

B	Ae^B	Particle density						
		2 g cm^{-3}		4 g cm^{-3}			8 g cm^{-3}	
		$Q_{rp} = 1.0$	$Q_{rp} = 1.5$	$Q_{rp} = 1.0$	$Q_{rp} = 1.5$	$Q_{rp} = 2.0$	$Q_{rp} = 1.0$	$Q_{rp} = 2.0$
50	10^6	28.5 - 28.9	28.5 - 28.9	29.4 - 29.9	29.7 - 30.2	.	.	.
	10^8	12.7 - 12.9	12.9 - 13.1	14.6 - 14.8	15.1 - 15.3	.	.	.
100	10^6	65.7 - 68.1	65.8 - 68.3	65.8 - 68.2	66.0 - 68.4	.	.	.
	10^8	62.7 - 64.8	62.7 - 64.9	62.8 - 64.9	63.0 - 64.9	.	.	.
150	10^6	.	.	74.8 - 78.9	.	75.0 - 79.0	74.9 - 78.9	75.1 - 78.9
	10^8	.	.	72.9 - 76.8	.	73.1 - 76.8	73.0 - 76.8	73.2 - 76.8
200	10^6	.	.	79.0 - 83.8	.	79.2 - 84.0	79.1 - 83.8	79.2 - 83.8
	10^8	.	.	77.6 - 82.3	.	77.8 - 82.4	77.7 - 82.3	77.8 - 82.5

Table XXIV. The range of the angles of crossing (deg) at expulsion at 1 AU from the sun for B = 150 and $e_o = 0$

Initial particle radius a (micron)	Ae^B	Particle density			
		4 g cm^{-3}		8 g cm^{-3}	
		$Q_{rp} = 1.0$	$Q_{rp} = 2.0$	$Q_{rp} = 1.0$	$Q_{rp} = 2.0$
1	10^6	74.8 - 78.9	75.0 - 79.0	74.9 - 78.9	75.1 - 78.9
	10^8	72.9 - 76.8	73.1 - 76.8	73.0 - 76.8	73.2 - 76.8
5	10^6	74.9 - 79.0	75.1 - 79.1	74.9 - 78.9	75.1 - 79.2
	10^8	73.0 - 77.2	73.2 - 76.8	73.0 - 77.1	73.3 - 77.0
10	10^6	74.9 - 78.9	75.1 - 79.2	74.9 - 78.8	75.2 - 79.5
	10^8	73.0 - 77.1	73.3 - 77.0	73.1 - 77.5	73.2 - 77.0

Table XXV. The range of the angles of crossing (deg) at expulsion at 1 AU from the sun for a = 1 micron and B = 150

Initial orbital eccentricity e_o	Ae^B	Particle density			
		4 g cm^{-3}		8 g cm^{-3}	
		$Q_{rp} = 1.0$	$Q_{rp} = 2.0$	$Q_{rp} = 1.0$	$Q_{rp} = 2.0$
0.0	10^6	74.8 - 78.9	75.0 - 79.0	74.9 - 78.9	75.1 - 78.9
	10^8	72.9 - 76.8	73.1 - 76.8	73.0 - 76.8	73.2 - 76.8
0.1	10^6	75.3 - 78.2	75.4 - 78.2	75.5 - 78.4	75.6 - 78.3
	10^8	73.4 - 76.1	73.5 - 76.0	73.5 - 76.4	73.7 - 76.1
0.2	10^6	75.4 - 78.1	75.4 - 78.0	75.5 - 78.3	75.7 - 78.1
	10^8	73.5 - 75.8	73.5 - 75.8	73.6 - 76.1	73.7 - 75.9

Table XXVI. The range of the intercept angles (deg) at expulsion at 1 AU from the sun for a = 1 micron and $e_o = 0$

B	Ae^B	Particle density						
		2 g cm^{-3}		4 g cm^{-3}			8 g cm^{-3}	
		$Q_{rp} = 1.0$	$Q_{rp} = 1.5$	$Q_{rp} = 1.0$	$Q_{rp} = 1.5$	$Q_{rp} = 2.0$	$Q_{rp} = 1.0$	$Q_{rp} = 2.0$
50	10^6	29.0 - 30.1	24.7 - 25.6	33.2 - 34.5	31.4 - 32.5	.	.	.
	10^8	17.2 - 17.9	14.1 - 14.7	22.0 - 23.1	21.1 - 21.9	.	.	.
100	10^6	34.4 - 38.5	31.2 - 35.2	36.7 - 40.7	35.2 - 39.2	.	.	.
	10^8	36.3 - 39.8	32.8 - 36.2	38.5 - 42.0	37.2 - 40.5	.	.	.
150	10^6	.	.	35.2 - 45.3	.	32.7 - 42.6	35.9 - 46.0	34.5 - 44.2
	10^8	.	.	36.7 - 45.4	.	34.5 - 42.5	37.6 - 46.2	36.6 - 44.7
200	10^6	.	.	34.6 - 52.0	.	31.9 - 49.9	34.7 - 52.5	33.8 - 51.0
	10^8	.	.	36.1 - 51.0	.	33.7 - 48.7	36.8 - 51.7	35.3 - 50.6

Table XXVII. The range of the intercept angles (deg) at expulsion at 1 AU from the sun for B = 150 and $e_o = 0$

Initial particle radius a (micron)	Ae^B	Particle density			
		4 g cm^{-3}		8 g cm^{-3}	
		$Q_{rp} = 1.0$	$Q_{rp} = 2.0$	$Q_{rp} = 1.0$	$Q_{rp} = 2.0$
1	10^6	35.2 - 45.3	32.7 - 42.6	35.9 - 46.0	34.5 - 44.2
	10^8	36.7 - 45.4	34.5 - 42.5	37.6 - 46.2	36.6 - 44.7
5	10^6	36.1 - 46.5	35.4 - 45.4	35.7 - 45.8	35.6 - 45.8
	10^8	37.4 - 47.0	37.3 - 45.5	38.2 - 47.5	37.7 - 46.2
10	10^6	35.7 - 45.8	35.6 - 45.8	37.0 - 46.8	34.9 - 46.0
	10^8	38.2 - 47.5	37.7 - 46.2	38.0 - 48.3	36.6 - 45.1

Table XXVIII. The range of the intercept angles (deg) at expulsion at 1 AU from the sun for a = 1 micron and B = 150

Initial orbital eccentricity e_o	Ae^B	Particle density			
		4 g cm^{-3}		8 g cm^{-3}	
		$Q_{rp} = 1.0$	$Q_{rp} = 2.0$	$Q_{rp} = 1.0$	$Q_{rp} = 2.0$
0.0	10^6	35.2 - 45.3	32.7 - 42.6	35.9 - 46.0	34.5 - 44.2
	10^8	36.7 - 45.4	34.5 - 42.5	37.6 - 46.2	36.6 - 44.7
0.1	10^6	48.3 - 55.2	44.6 - 51.4	50.0 - 57.0	48.0 - 54.7
	10^8	49.4 - 55.2	45.9 - 51.5	50.8 - 57.0	49.3 - 54.6
0.2	10^6	49.8 - 56.1	46.1 - 52.4	51.5 - 58.0	49.8 - 55.7
	10^8	51.2 - 56.2	47.2 - 52.3	52.8 - 58.0	50.9 - 55.7

Table XXIX. The expulsion lifetime (yr) for a = 1 micron and $e_o = 0$

B	Ae^B	Particle density						
		2 g cm^{-3}		4 g cm^{-3}			8 g cm^{-3}	
		$Q_{rp} = 1.0$	$Q_{rp} = 1.5$	$Q_{rp} = 1.0$	$Q_{rp} = 1.5$	$Q_{rp} = 2.0$	$Q_{rp} = 1.0$	$Q_{rp} = 2.0$
50	10^6	1300	1100	1500	1200	.	.	.
	10^8	1900	2100	2200	1800	.	.	.
100	10^6	53	49	73	81	.	.	.
	10^8	82	77	96	89	.	.	.
150	10^6	.	.	12	.	9.5	14	12
	10^8	.	.	20	.	13	21	19
200	10^6	.	.	3.1	.	3.1	4.1	3.6
	10^8	.	.	4.8	.	4.1	5.8	6.3

Table XXX. The expulsion lifetime (yr) for B = 150 and $e_o = 0$

Initial particle radius a (micron)	Ae^B	Particle density: 4 g cm^{-3}		8 g cm^{-3}	
		$Q_{rp} = 1.0$	$Q_{rp} = 2.0$	$Q_{rp} = 1.0$	$Q_{rp} = 2.0$
1	10^6	12	9.5	14	12
	10^8	20	13	21	19
5	10^6	17	16	20	18
	10^8	30	22	29	27
10	10^6	20	18	26	25
	10^8	29	27	45	31

Table XXXI. The expulsion lifetime (yr) for a = 1 micron and B = 150

Initial orbital eccentricity e_o	Ae^B	Particle density: 4 g cm^{-3}		8 g cm^{-3}	
		$Q_{rp} = 1.0$	$Q_{rp} = 2.0$	$Q_{rp} = 1.0$	$Q_{rp} = 2.0$
0.0	10^6	12	9.5	14	12
	10^8	20	13	21	19
0.1	10^6	12	9.4	15	14
	10^8	16	15	29	17
0.2	10^6	16	16	20	15
	10^8	21	23	30	22

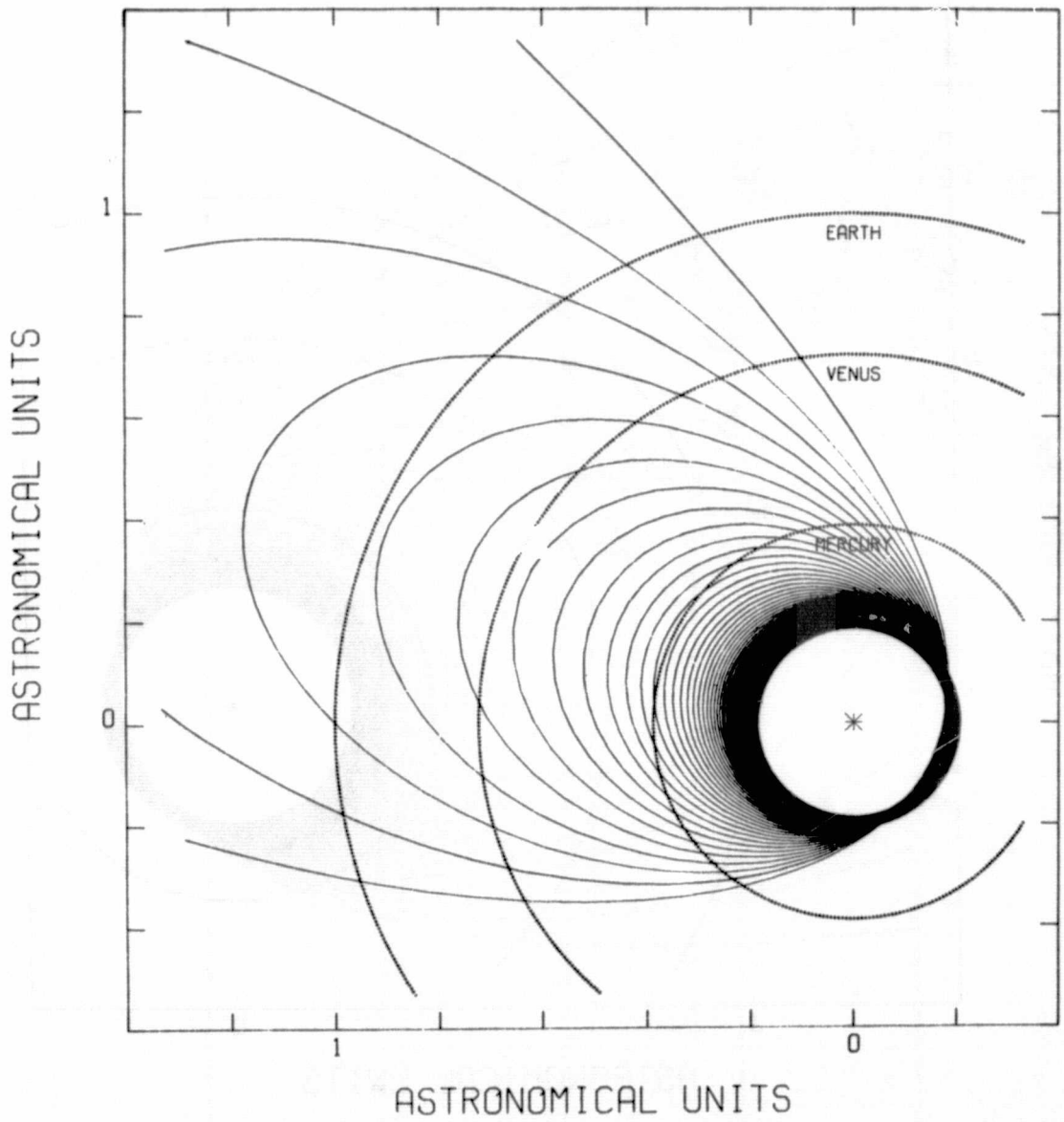

Figure 1. A computer plot of the orbital evolution of a vaporizing dust particle. Initial conditions: $\xi = 0.1$, a = 1 micron, $\rho = 2$ g cm^{-3}, $Q_{rp} = 1$, $B = 100$, $Ae^{B} = 10^{6}$, $e_o = 0$.

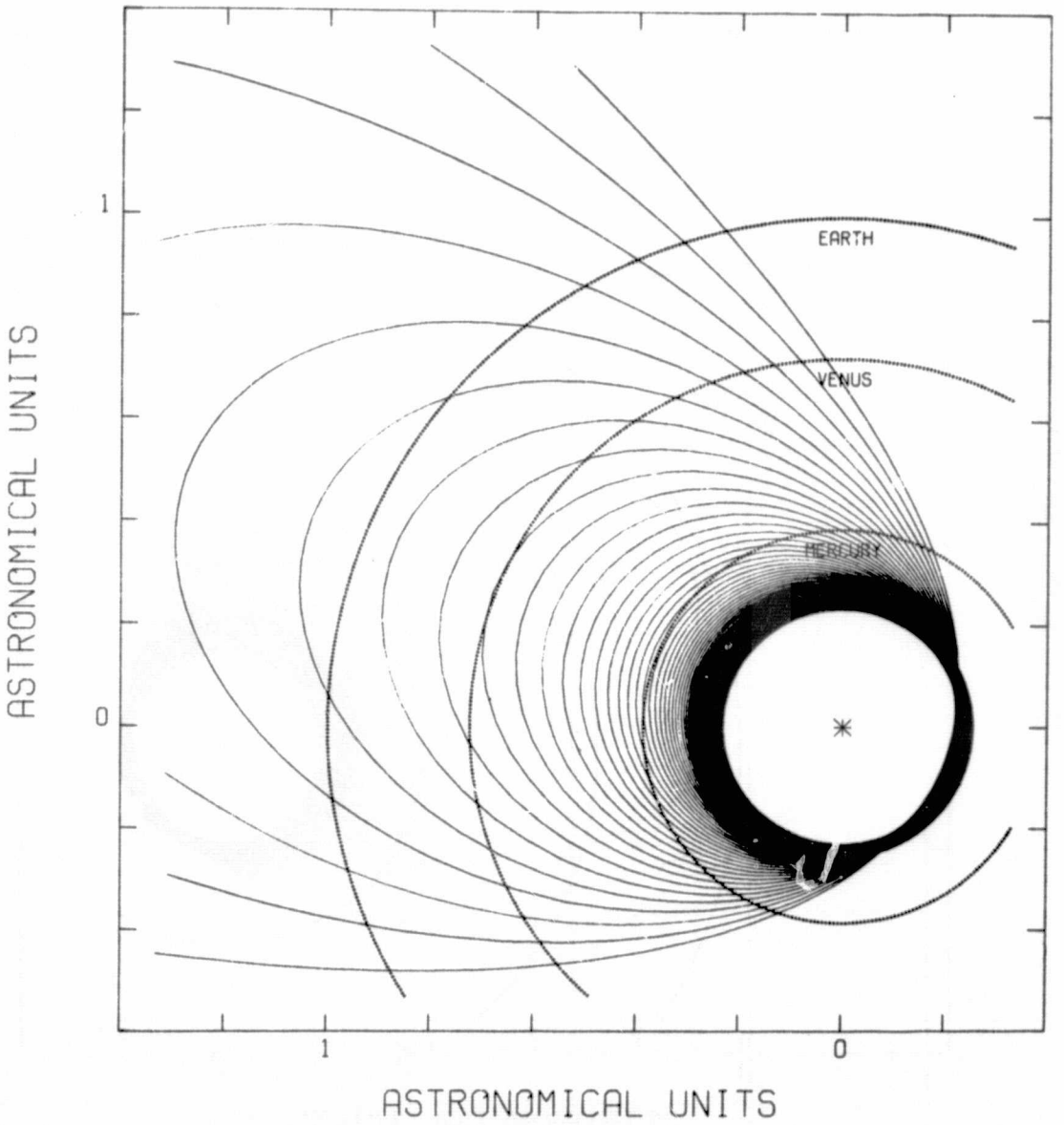

Figure 2. A computer plot of the orbital evolution of a vaporizing dust particle. Initial conditions: $\xi = 0.1$, a = 1 micron, $\rho = 2$ g cm^{-3}, $Q_{rp} = 1$, B = 100, $Ae^{B} = 10^{8}$, $e_o = 0$.

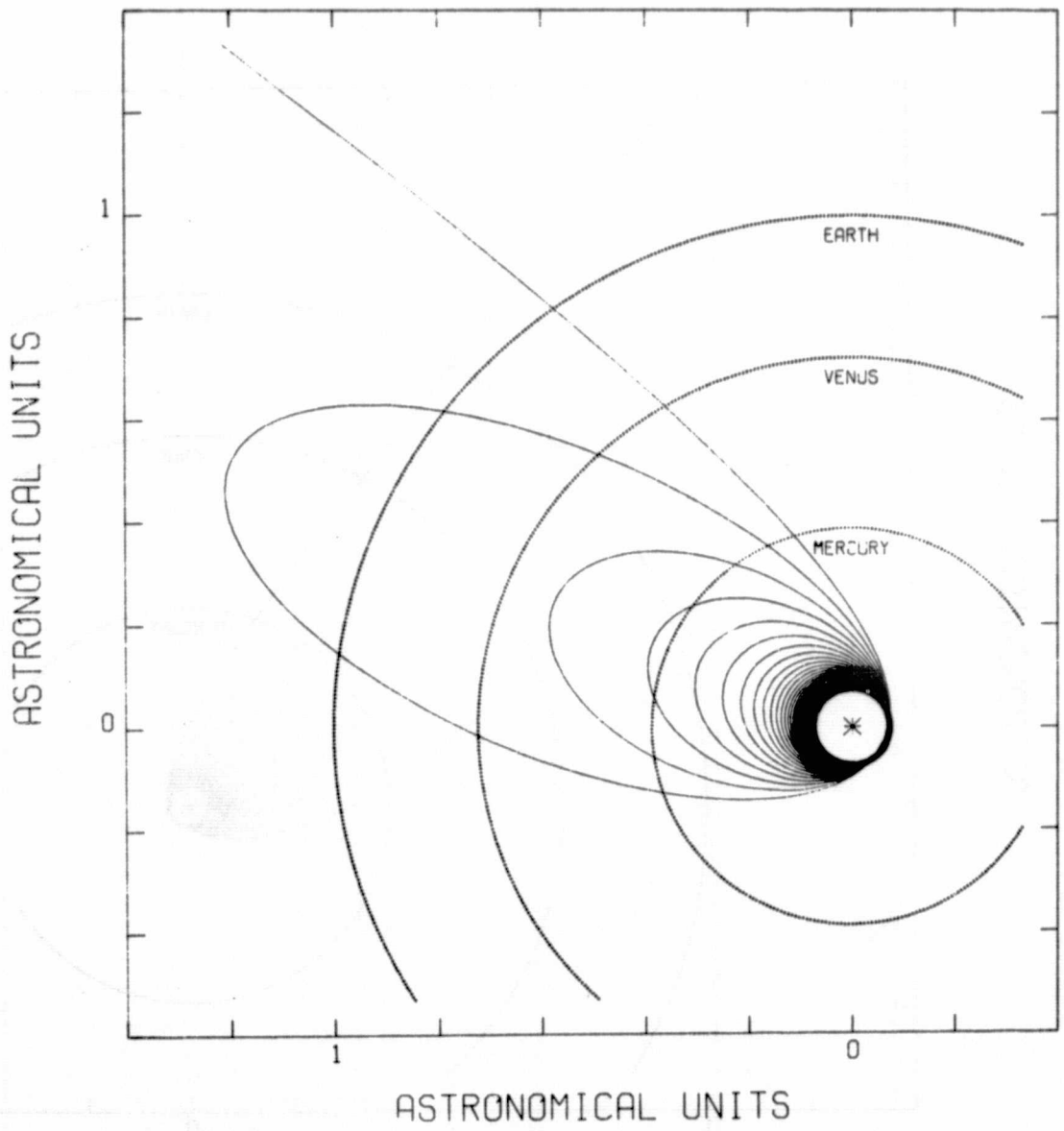

Figure 3. A computer plot of the orbital evolution of a vaporizing dust particle. Initial conditions: $\xi = 0.1$, a = 1 micron, $\rho = 8$ g cm^{-3}, $Q_{rp} = 1$, B = 150, $Ae^{B} = 10^{6}$, $e_o = 0$.

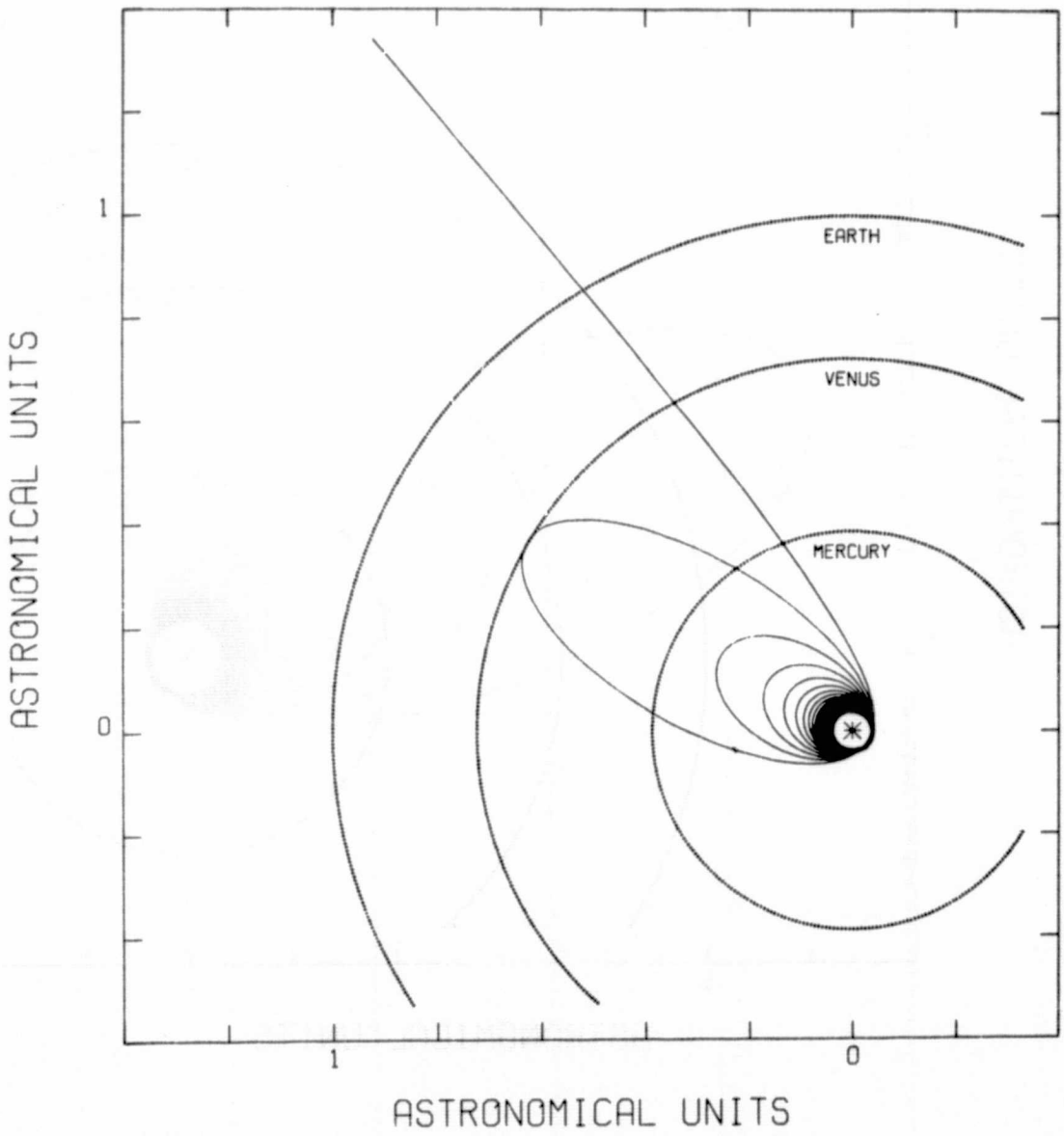

Figure 4. A computer plot of the orbital evolution of a vaporizing dust particle. Initial conditions: $\xi = 0.1$, a = 1 micron, $\rho = 8$ g cm^{-3}, $Q_{rp} = 1$, B = 200, $Ae^{B} = 10^{6}$, $e_o = 0$.

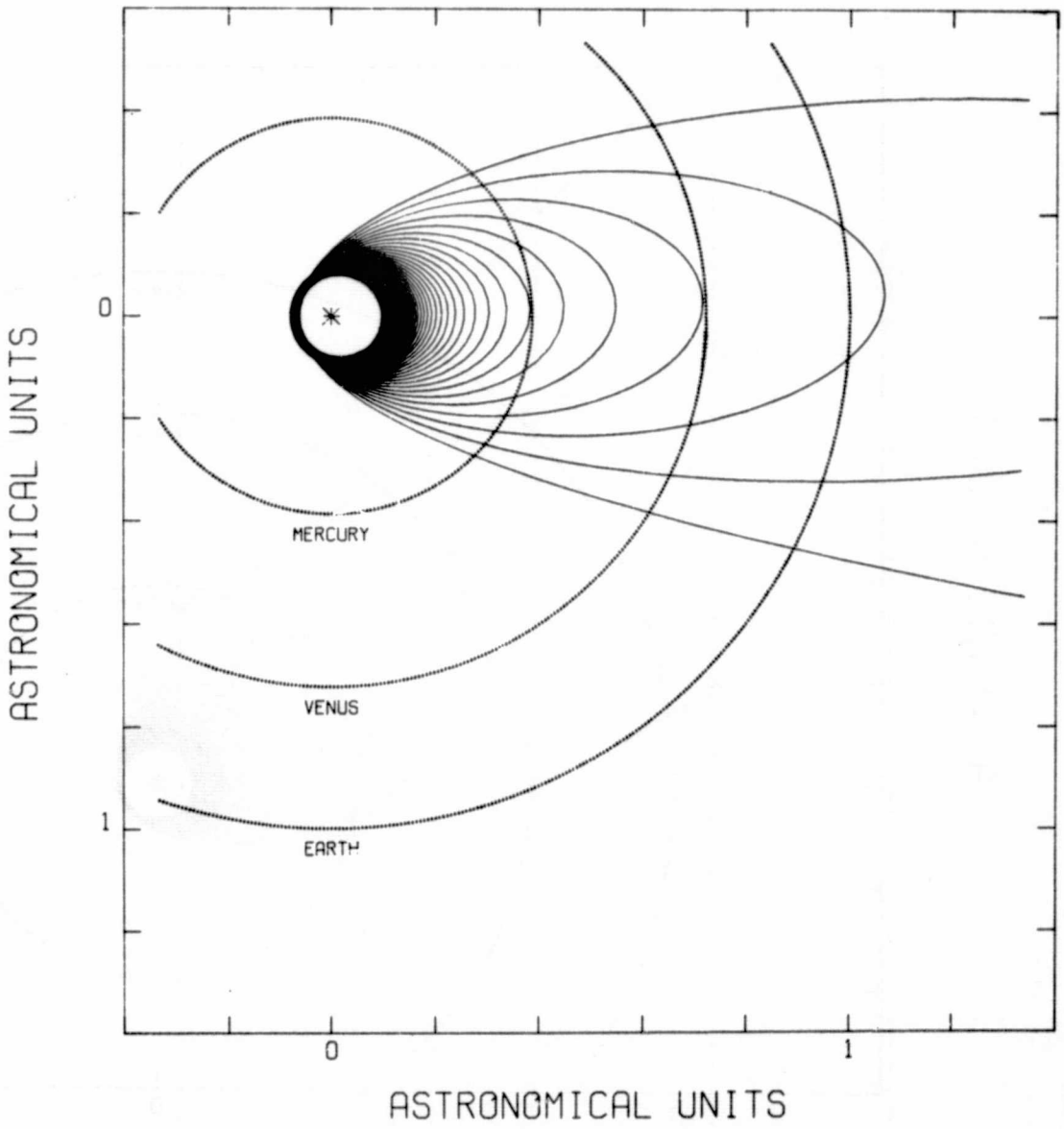

Figure 5. A computer plot of the orbital evolution of a vaporizing dust particle. Initial conditions: $\xi = 0.1$, a = 1 micron, $\rho = 8$ g cm^{-3}, $Q_{rp} = 1$, $B = 150$, $Ae^{B} = 10^{6}$, $e_o = 0.2$.

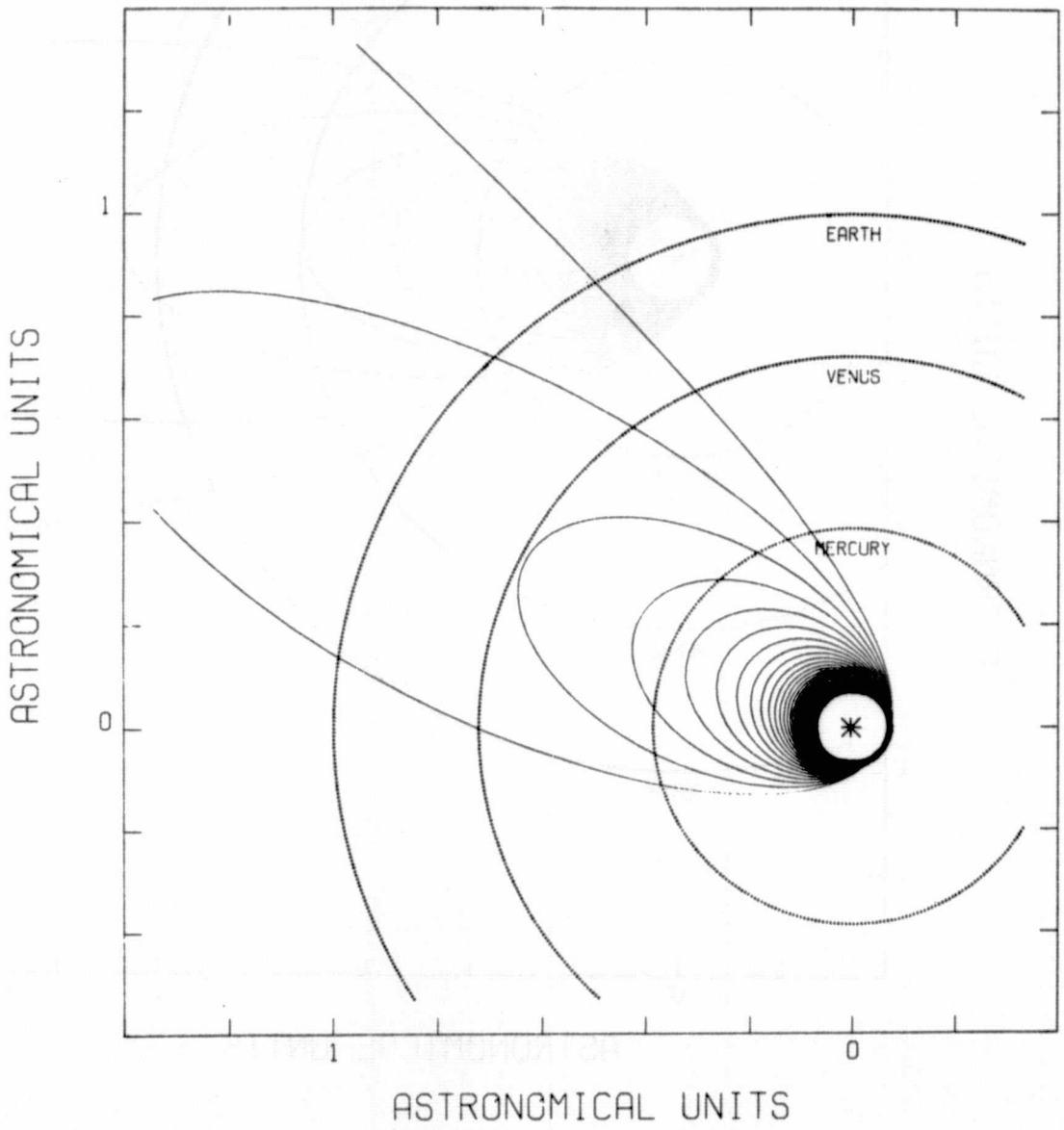

Figure 6. A computer plot of the orbital evolution of a vaporizing dust particle. Initial conditions: $\xi = 0.1$, a = 10 microns, $\rho = 8$ g cm^{-3}, $Q_{rp} = 1$, $B = 150$, $Ae^{B} = 10^{6}$, $e_o = 0$.

the outer edge of the thick ring, the particle then spirals — due to the prevailing Poynting-Robertson effect — down to the inner edge of the ring. At that time the perihelion distance still slightly decreases until it stabilizes, while the eccentricity starts increasing progressively, resulting ultimately in the particle's expulsion.

Work is in progress on an extensive paper summarizing the results of this investigation.

IV. References

Sekanina, Z. (1975). A study of the icy tails of the distant comets. Icarus 25, 218-238.

Sekanina, Z., and Miller, F. D. (1975). On the nature of the anti-tail of Comet Kohoutek (1973f). II. Comparison of the working model with ground-based photographic observations. Center for Astrophys. Preprint Series No. 312. Submitted to Icarus.

PART C. OTHER ACTIVITIES IN THE REPORTED PERIOD

I. Statistical investigation of anomalous tails of comets

Work continued on the study of heavy dust particles in cometary tails (anomalous tails or antitails). The results of the statistics of the anomalous tails were presented at the IAU Colloquium No. 31 "Interplanetary Dust and Zodiacal Light", held at Heidelberg, Germany, last June (see Addendum II).

During my recent visit to the Lunar and Planetary Laboratory of the University of Arizona in Tucson, Dr. E. Roemer and I examined comet images on a number of her plates for a possible presence of faint antitails. The results of inspection of the images of P/Encke in 1964 were included in the written version of my Heidelberg paper (see p. II-2 of Addendum II).

II. Band structures in the dust tails of Comets 1957 V and 1910 I

Comets 1957 V (≡ 1957d, Mrkos) and 1910 I (≡ 1910a) have so far been the best examples of comets that show peculiar band structures in the dust tail. The structures are short-lived phenomena (a typical lifetime of several days), are often difficult to discriminate clearly from the smooth background of the tail dust, and might be a result of particle fragmentation in cometary tails (Sekanina 1974).

For an anticipated extensive study of these formations in the tail of Comet 1957 V, the photographic material was acquired in the reported period from the following observers: John A. Farrell, now with the Los Alamos

Scientific Laboratory, Los Alamos, New Mexico, who photographed the bands at Fort Worth, Texas, on 1957 August 14.1, 15.1, 16.1 and 17.1 (UT) with a 19-cm f/1.5 Schmidt camera using a Royal Pan film; Alan McClure, Hollywood, California, observing from Frazier Mountain, near Frazier Park, California, on August 10.2, 11.2, 12.2 and 14.2 with a 10-cm f/5 camera and using 103a-E plates and a filter; and Henry L. Giclas, Lowell Observatory, Flagstaff, Arizona, who used the Observatory's 33-cm f/5.1 astrograph and a 103a-O plate on August 16.2.

The photographs of Comet 1910 I, to be used for an analogous study, were obtained by C. O. Lampland, Lowell Observatory, with the Observatory's Voigtlander 3.7-cm f/5.4 camera on two different emulsions, and copies of the plates from 1910 January 27.1, 28.1, 29.1 and 30.1 (UT), showing the bands, were acquired courtesy of Mr. Giclas.

III. Review of the progress in the studies of cometary dust tails for the triennial report of the IAU Commission 15

At the request of Professor A. H. Delsemme, Department of Physics and Astronomy, The University of Toledo, currently the President of Commission 15 of the International Astronomical Union (The Physical Study of Comets, Minor Planets and Meteorites), I prepared a review paper on the dust tails of comets for the 1973-75 triennial report of the Commission. The review is attached as Addendum III.

IV. Lectures and seminars

During the reported period I gave talks on the dust tails and antitails of comets to three professional audiences: at the Institut d'Astrophysique,

Université de Liège, Cointe-Ougrée, Belgium, on June 23, 1975; at the meeting of the British Astronomical Association, held in London, England, on June 25, 1975 (Miles et al. 1975); and at the Lowell Observatory, Flagstaff, Arizona, on August 22, 1975.

V. References

Miles, H. G., Stone, G. E., and Hatfield, H. R. (1975). Ordinary meeting of the Association. Journ. Brit. Astron. Assoc. 85 (in press).

Sekanina, Z. (1974). Progress in our understanding of cometary dust tails. In The Study of Comets, IAU Colloq. No. 25 (in press).

PART D. PLANS FOR THE NEXT PERIOD (SEPTEMBER 15, 1975 TO MARCH 14, 1976)

1. A major task is the study of the band structures in the dust tails of the two comets, 1957 V and 1910 I (see Part C, Section II). Each band will first have to be identified on a sequence of photographs and then its motion through the tail can be studied. However, since none of the photographs was calibrated photometrically, the intensity distribution in the bands cannot unfortunately be determined.
2. Also of high priority is the statistical study of the antitails of comets. This paper, near completion, will also give predictions for favorable conditions to observe antitails in the future returns of the short-period comets.
3. Although the study of the Cerro Tololo observations has indicated a fair degree of similarity with the working model of the antitail of Comet Kohoutek, calculated by the writer from the qualitative and semi-quantitative descriptions of the antitail as available by mid-1974, an improved model of the antitail is clearly needed.
4. The study of the antitail of Comet Kohoutek 1973 XII should be complemented by a similar study of the antitail of Comet Arend-Roland 1957 III. Three high-quality plates of Comet Arend-Roland, which are calibrated photometrically, are available from the collection of Dr. F. D. Miller, University of Michigan.
5. The study of the orbital evolution of vaporizing dust particles has essentially been completed. To write up a paper, covering basically the contents of Part A of the Semiannual Report No. 7 and Part B of the present Report, is all that remains to be done in this respect.

It is not expected that all the above problems will be settled by the end of the next semiannual period, but efforts will be made to run the project most efficiently.

ADDENDUM I

To appear in
Interplanetary Dust and Zodiacal Light
Proceedings from IAU Colloquium No. 31
Heidelberg, Germany, 10-13 June 1975

MODELING OF THE ORBITAL EVOLUTION OF VAPORIZING DUST PARTICLES NEAR THE SUN

Zdenek Sekanina
Center for Astrophysics
Harvard College Observatory and Smithsonian Astrophysical Observatory
Cambridge, Massachusetts 02138, U.S.A.

The Poynting-Robertson (P-R) effect (Robertson, 1937, Wyatt and Whipple, 1950), assisted by a pseudo P-R effect due to the sputtering (Whipple, 1955, 1967), is known to cause small dust particles in interplanetary space to spiral toward the sun. Evaporation from the surface of such particles thus increases progressively with time and their size is being reduced accordingly. When the rate of evaporation is no longer negligibly low, it induces on the particle a measurable dynamical effect, which is associated with the implied variations in the magnitude of solar radiation pressure relative to solar attraction. By gradually reducing solar attraction, the particle evaporation tends to increase the orbit dimensions, thus acting against P-R. The P-R inward spiraling, far exceeding the dynamical effect from evaporation at larger heliocentric distances, slows gradually down as the particle approaches the sun, and virtually ceases when the critical distance is reached, where the two forces approximately balance each other. Then, typically, the perihelion distance stabilizes, while the eccentricity starts increasing very rapidly until the particle is swept out of the solar system. This, in brief, is the orbital evolution of a vaporizing particle in the absence of other potentially important but rather poorly known processes, such as particle collisions, rotational bursting, electric charging and interactions with the solar wind and with the interplanetary magnetic field.

If we assume that the particle is rapidly rotating, spherical in shape, of a uniform density ρ, and that most of the solar energy it absorbs is spent on reradiation, the linear vaporization rate of the particle $\dot{a}$ is given, in the first approximation, by

$$\dot{a} = (A/\rho)\ \exp[B(1-r^{\frac{1}{2}})],$$

where A is the normalized (to 1 AU from the sun) vaporization flux from the particle (mass per unit surface area per unit of time), r is the heliocentric distance (in AU), $B = 1.81\ L\ (\varepsilon/\kappa)^{\frac{1}{4}}$, L is the latent heat of vaporization (in kcal $mole^{-1}$), κ is the absorptivity of the particle's surface for solar radiation and ε its emissivity for reradiation. In the following the expression $L\ (\varepsilon/\kappa)^{\frac{1}{4}}$ will be termed the effective latent heat of vaporization.

The calculations based on this model of particle evaporation indicate that a particle, whose pre-evaporation orbit was circular, is expelled from the solar system on a hyperbolic orbit as soon as radiation pressure attains about 0.8 of solar attraction. The expulsion limit, however, is lower for elongated pre-evaporation orbits; it amounts, for example, only to 0.5 - 0.6 of solar attraction for the pre-evaporation eccentricity of 0.2. Nevertheless, purely dielectric particles, some of which may never be subject to radiation pressure exceeding 0.5 of solar gravity, could perhaps, under certain circumstances, vaporize off completely near the sun. However, this possibility is not here pursued further, as it is considered rather untypical.

In order to determine quantitatively the relation between the initial (pre-evaporation) and final (at expulsion) physical and dynamical characteristics of the vaporizing particles, we computed a total of 64 runs, varying the initial particle size and density, the effective latent heat of vaporization and the normalized vaporization flux, the scattering efficiency for radiation pressure and the eccentricity of the initial orbit. We arrived at the following basic conclusions.

The final particle size is on the order of magnitude of 0.1 micron. It is essentially independent of the initial particle size, the effective latent heat of vaporization and the normalized vaporization flux. It is directly proportional to the scattering efficiency for radiation pressure, inversely proportional to the particle density and it increases with increasing eccentricity of the initial orbit.

The perihelion distance of the final orbit varies in inverse proportion to an approximately 2.2 power of the effective latent heat, from less than 0.1 AU above 70 kcal $mole^{-1}$ to more than 1 AU below 25 kcal $mole^{-1}$, and it decreases with decreasing normalized vaporization flux.

It is, however, virtually independent of the initial particle size, its density and the scattering efficiency, and only slightly dependent on the initial eccentricity.

The heliocentric velocity at expulsion can lie anywhere between the parabolic limit and a maximum hyperbolic velocity, which is determined by the final perihelion distance, the two vaporization constants, the scattering efficiency, the particle density and the final particle size. However, since the particles are strongly affected by radiation pressure, their velocity of escape from the solar system and the maximum hyperbolic velocity are, at 1 AU from the sun, typically less than 20 and 30 km s^{-1}, respectively. The velocities are somewhat higher than indicated for more eccentric initial orbits and for materials of the effective latent heat of vaporization exceeding 100 kcal $mole^{-1}$.

The maximum intercept velocity at expulsion, i.e., the maximum velocity of an expelled particle relative to the earth at the encounter, increases with increasing effective latent heat of vaporization, but attains no more than 40 km s^{-1} at 100 kcal $mole^{-1}$.

The maximum intercept angle at expulsion, i.e., the maximum angle toward the sun subtended by the direction from which the particle intercepts the earth and by the earth's apex direction, also increases with increasing effective latent heat, reaching about 50° at 100 kcal $mole^{-1}$.

Finally, the expulsion lifetime of a vaporizing particle, measured by the span of time from the onset of appreciable evaporation to expulsion, decreases from some 1000 years at the effective latent heat of 30 kcal $mole^{-1}$ to about 10 years at 100 kcal $mole^{-1}$. The lifetime increases somewhat with the initial particle size and the particle density.

This research was supported by a grant NGR 09-015-159 from the National Aeronautics and Space Administration.

References

Robertson, H. P. (1937), Mon. Not. Roy. Astron. Soc., 97, 423.
Whipple, F. L. (1955), Astrophys. J., 121, 750.
Whipple, F. L. (1967), in "The Zodiacal Light and the Interplanetary Medium", Weinberg, J.L., Ed., NASA SP-150, Washington, D.C., p. 409.
Wyatt, S. P., and Whipple, F. L. (1950), Astrophys. J., 111, 134.

ADDENDUM II

To appear in
Interplanetary Dust and Zodiacal Light
Proceedings from IAU Colloquium No. 31
Heidelberg, Germany, 10-13 June 1975

PREDICTED FAVORABLE VISIBILITY CONDITIONS FOR ANOMALOUS TAILS OF COMETS

Zdenek Sekanina
Center for Astrophysics
Harvard College Observatory and Smithsonian Astrophysical Observatory
Cambridge, Massachusetts 02138, U.S.A.

It was shown elsewhere (Sekanina, 1974) that the observability from the earth of an anomalous tail (antitail) of a comet can be rather straightforwardly predicted from the dynamical and geometric conditions. The physical presence or absence of the antitail at a precalculated time is then a measure of the comet's production rate, at the relevant emission times, of relatively heavy dust particles (mostly of submillimeter size) that constitute such an antitail. Because the large grains are emitted from the nucleus at very low velocities (typically meters or tens of meters per second), an antitail is essentially a two-dimensional formation in the orbit plane of the comet and can be recognized best when projected edge-on, i.e., when the earth crosses the nodal line of the comet's orbit. In general, however, this condition is not essential for the recognition of antitails (cf., e.g., Comet Kohoutek 1973 XII).

Since the emission rate of heavy dust particles is a potentially significant parameter for a physical classification of comets, we made use of the visibility conditions to list the comets that should have displayed a sunward tail around the time of the earth's passages through the orbit plane. This type of the antitail observability will be termed the nodal appearance. A computer program executing the conditions for a nodal appearance was applied to the Catalogue of Cometary Orbits (Marsden, 1975), starting with the comets of 1737. However, we excluded all comets that were at the critical times located near the antisolar point in the sky (elongations exceeding 135°), where the definition of the sunward direction becomes meaningless. We also excluded all cases at heliocentric distances larger than 2 AU in order not to confuse the antitails with the icy tails (Sekanina, 1973, 1975) that are observed far from the sun and point fairly frequently in the general direction of the sun.

The statistics of the nodal appearances of antitails of comets, whose conditions were satisfied within, or not more than 5 days outside, the period of observation, are listed in Table I, separately for nearly-parabolic comets (revolution periods more than 200 years) and for short-period comets. The calculations were done for dust particles with a ratio $1-\mu$ of radiation pressure to solar gravity of 0.01 (known to be common in observed antitails) and for two different starting emission times. Whereas the choice of $1-\mu$ is not crucial, Table I shows that the time of onset of dust production affects the statistics substantially. The comets with a sunward tail reported to have been detected near the predicted time are listed in Table II, where columns 2 to 4 give, respectively, the perihelion distance, the reciprocal value of the original semimajor axis (for P/Encke the revolution period), derived from Marsden (1975) and from Everhart and Raghavan (1970), and the absolute magnitude (Vsekhsvyatsky, 1958). We remark that with the exception of 1937 IV the comets have perihelia well inside the earth's orbit, and that apart from the controversial case of P/Encke (see details below) the comets' revolution periods are longer than 7000 years and their absolute magnitudes brighter than 8.

Table I points consistently to a conclusion that only about 20 to 30% of the nearly-parabolic comets that should have displayed an antitail at the node were actually observed to do so. Indeed, if we count only the comets with nearly-ideal observing conditions, the figure is 22% for the onset of emission at 4 AU and increases to 30%, if the condition is relaxed to 2 AU. If we count all comets that were observed near the node, the fraction of positive observations is lower, as can be expected, but not very substantially: we find 19% for 4 AU emissions and 23% for 2 AU emissions.

The results are dramatically different for short-period comets. Although there were numerous opportunities for observing a nodal appearance of an antitail, we do not yet have a single clearly positive observation. The only promising case so far is that of P/Encke in 1964, for which Roemer (Roemer and Lloyd, 1966) secured a pair of plates only 2.5 days after the earth's nodal passage; the comet was 88 days after perihelion. A close inspection of the plates by Dr. Roemer and the writer revealed two extensions emanating from the weak, nearly stellar image of the comet in the opposite directions, one of them pointing right toward the sun. Although this sunward tail does not, in the writer's opinion, resemble the gas jets, frequently observed in P/Encke before perihelion, there is still no more than a 50% chance that it is a true antitail.

Table I. Statistics of predicted nodal appearances of antitails of comets in the past ($1-\mu = 0.01$)

Comets	Nearly-parabolic		Short-period	
Assumed sun-comet distance at ejection (before/at perihelion)	4 AU	2 AU	2 AU	Perihelion
(A) Number of comets (apparitions) whose predicted nodal appearances of antitail lie within the observed arc of orbit	69	45	21 (32)	6 (7)
(B) Number of comets (apparitions) under (A) that were observed near the node	48	30	16 (23)	6 (7)
(C) Number of comets (apparitions) under (B) with significant predicted characteristic length of antitail	38	28	15 (20)	2 (2)
(D) Number of comets (apparitions) under (C) with elongations exceeding 30° from the sun at the node	30	20	15 (19)	2 (2)
(E) Number of comets (apparitions) under (D) that were free from severe moonlight interference at the node	18	10	7 (10)	2 (2)
(F) Number of comets (apparitions) under (B) whose antitail was actually observed	9	7	1?(1)?	1?(1)?
(G) Number of comets (apparitions) under (E) whose antitail was actually observed	4	3	1?(1)?	1?(1)?

Table II. Comets with antitails observed at node

Comet	q (AU)	$(1/a)_{orig}$ $(AU)^{-1}$	H_{10} (mag)	Date of node crossing	Antitail seen	Conditions at node and remarks
1823	0.23	.	4.2	1824/1/24	1/22-25, 27, 31	Very favorable conditions
1844 II	0.86	+0.001007	4.9	1844/10/25	11/3, 8	Close to sun; moonlight interfering
1844 III	0.25	+0.002592	4:9	1845/1/18	1/11, 16, 25, 27	Moonlight interfering
1895 IV	0.19	-0.000168	5.2	1896/2/9	2/15, 19-21	Close to sun
1937 IV	1.73	+0.000063	6.0	1937/7/31	7/30, 8/1	Favorable; but early emissions only
1954 VIII	0.68	+0.000051	7.0	1954/7/25	7/30, 8/1, 3, 6-7	Node crossed 3 days before discovery
1957 III	0.32	+0.000009	5.4	1957/4/25	4/22-30	Very favorable conditions
1961 V	0.04	+0.002211	7.5	1961/7/21	7/25-26, 8/1	Node crossed 2 days before discovery; close to sun; moonlight interfering
1964 IV	0.34	(3.30 yr)	13-15	1964/8/27	8/30	P/Encke; nature of tail not clear
1969 IX	0.47	+0.000507	5.8	1970/1/2	12/26-28, 30-31, 1/2	Antitail short; early emissions only

The general absence of antitails among the short-period comets appears to be incompatible with the existence of meteor streams known to be associated with many of these comets. Unfortunately, at their observed returns, the parent comets of the three spectacular-storm producing meteor streams – P/Biela, P/Giacobini-Zinner and P/Tempel-Tuttle – were never placed favorably enough for a nodal appearance of an antitail. And, of all the other comets known to be related to meteor streams, only two had such very favorable apparitions: P/Encke in 1878, 1888 and 1964, and P/Pons-Winnecke in 1909, although P/Pons-Winnecke is not apparently associated with a permanent stream (Cook, 1973). The other comets with favorable conditions were P/Tempel 1 in 1867, P/Finlay in 1919, P/Kopff in 1945, P/Grigg-Skjellerup in 1947, and P/Schaumasse in 1952 and 1960. Streams that could be associated with P/Finlay or P/Grigg-Skjellerup have never been reported; the other comets have perihelia well beyond 1 AU.

With one doubtful and two negative results in the three nearly-ideal returns, P/Encke presents probably the most solid evidence to date against the positive correlation between the antitails and the meteor streams. In order to obtain more data, positive or negative, on the occurrence of the antitails, we investigated their visibility conditions in the future returns of the short-period comets. Among 166 returns of 60 comets with perihelia within 2 AU between 1976 and 1999 (orbital elements courtesy of Dr. Marsden), the following instances – most of them outside nodal areas – are considered as most significant: P/d'Arrest in 1976/77, P/Encke in 1977 and 1987, P/Schwassmann-Wachmann 3 in 1979, P/Honda-Mrkos-Pajdušáková in 1980, P/Grigg-Skjellerup in 1982 and 1987, P/Crommelin in 1984, P/Pons-Winnecke in 1989/90, and P/Giacobini-Zinner in 1999.

This work was supported by grants NGR 09-015-159 and NSG 7082 from the National Aeronautics and Space Administration.

References

Cook, A. F. (1973), in "Evolutionary and Physical Properties of Meteoroids", Hemenway, C. L., Millman, P. M., and Cook, A. F., Eds., NASA SP-319, Washington, D.C., p. 183.
Everhart, E., and Raghavan, N. (1970), Astron. J. 75, 258.
Marsden, B. G. (1975), Catalogue of Cometary Orbits. (2nd edition.) IAU Central Bureau for Astronomical Telegrams, Smithsonian Astrophys. Obs.
Roemer, E., and Lloyd, R. E. (1966), Astron. J. 71, 443.
Sekanina, Z. (1973), Astrophys. Lett. 14, 175.
Sekanina, Z. (1974), Sky and Tel. 47, 374.
Sekanina, Z. (1975), Icarus 25, 218.
Vsekhsvyatsky, S. K. (1958), Physical Characteristics of Comets. (In Russian.) Moscow, p. 51. (English transl.: Jerusalem, 1964.) Follow-ups: Soviet Astron. 6, 849 (1963); 10, 1034 (1967); and 15, 310 (1971).

ADDENDUM III

DUST TAILS

A CONTRIBUTION TO THE 1973-75 TRIENNIAL REPORT OF IAU COMMISSION 15

Zdenek Sekanina

The tail and particularly the antitail of Comet Kohoutek (1973 XII) attracted most attention in the reported period. The appearance of a sunward tail shortly after perihelion had been predicted by Sekanina (1973a, 1974a), and was observed from Skylab III both visually (Gibson 1974a, b) and photographically (MacQueen et al. 1974) and from the ground in the infrared (Ney 1974a, b). A large number of ground-based photographic and visual observations of the tail and antitail were reported later in January and in February. Ney detected the silicate signature at 10 microns in the tail but not in the antitail, and concluded that the antitail particles must have definitely been larger than some 10 to 20 microns in diameter. Physico-dynamical models of the antitail were offered by Sekanina (1974b), who used the Finson-Probstein approach for the case of negligibly small emission velocities, by Gary and O'Dell (1974), who applied a simplified syndyne approach, and by Lamy and Koutchmy (1975). Sekanina and Gary and O'Dell found large particles present in the antitail, the estimates ranging from a few tens micron- to millimeter-sized grains, whereas Lamy and Koutchmy suggested a possibility of very tiny dust particles, typically 0.02 microns in radius, in order to explain the strongly polarized light of the antitail in mid-January 1974 (Bücher et al. 1975). Sekanina and Miller (1975) compared Sekanina's model with absolute photometric profiles measured from the plates taken at Cerro Tololo and confirmed that there was evidence for the

presence in the antitail of appreciably vaporizing dust particles. Spinrad and Smith (1973) argued in favor of the dust-grain evaporation in Comet Bennett (1970 II) in order to explain a 7000 km sunward offset between the peak of the sodium emission and that of the continuum.

The Finson-Probstein model of dust comets was further applied successfully to two more comets: Bennett (1970 II) and Seki-Lines (1962 III). For Bennett Sekanina and Miller (1973) found subkilometer-per-second particle emission velocities, particle sizes of typically a few microns, the dust production rate of 2×10^7 g/sec at 0.56 AU from the sun and the nucleus of the comet 2.6 km in radius. The cutoff of the particle size distribution in this comet was discussed by O'Dell (1974). For Seki-Lines Jambor (1973) obtained somewhat lower emission velocities and larger particle sizes, and found that a sharp variation in the production rate of dust at perihelion was the cause of the observed "split" tail (or the "shadow of the nucleus"). Whereas the Finson-Probstein approach was almost universally accepted, Wurm (1974) pointed out that its fundamental assumption of isotropy in the dust emission is incompatible with the frequent presence of sunward dust streamers in the inner coma of many comets. Benvenuti (1974) found that the dust structures near the nucleus vary from comet to comet.

Small dust particles (for which radiation pressure balances solar gravity) were reported to have been detected by the earth-orbiting satellite HEOS 2 (Hoffmann et al. 1974, Grün et al. 1975). An enhanced particle flux in the velocity range of 15 to 20 km/sec and mass range 10^{-13} to 10^{-11} grams, observed from mid-May until early August 1974, was apparently due to emissions from the comet at solar distances near or beyond 4 AU.

The behavior of the tails of many distant comets led Sekanina (1973b,

1975a) to a hypothesis of icy (or solid hydrate) grains, 0.01 cm in size and larger, as the material constituting these tails. The grains are apparently emitted from the nucleus at distances up to 15 AU from the sun, so that substances more volatile than water snow must be present in the nucleus at the large distances to supply the necessary momentum.

Patashnick and Rupprecht (1975) showed that the sublimation rate of pure icy grains in interplanetary space depends considerably on their size, with a deep minimum at a 50 micron diameter at solar distances comparable to the earth-sun distance.

Rieke and Lee (1974) and Rieke et al. (1974) concluded from their study of the infrared spectra of Comet Kohoutek (and others) that while silicates are the only material definitely identified in cometary dust, the composition of the dust varies from comet to comet and also with time for any particular comet. Comet Kohoutek was also measured in the infrared by Gatley et al. (1974) and by others. The 10 micron silicate signature and a particle color temperature higher than a black-body temperature were observed.

It was shown by Sekanina (1974a) that the appearance of an antitail of a comet can be rather straightforwardly predicted from the geometrical configuration, when one is reasonably sure of a sufficiently high concentration of submillimeter- to millimeter-sized meteoroids at sufficiently early emission times. His statistical study of the observed antitails (Sekanina 1975b) suggests that only 20 to 30 per cent of nearly-parabolic comets and no or essentially no short-period comets that should display an antitail actually do so; he also provided predictions to search for antitails of the short-period comets in their forthcoming returns.

Weinberg and Beeson (1975) found a very strong negative polarization of the light in the tail of Comet Ikeya-Seki (1965 VIII), which they interpreted in terms of slightly absorbing submicron dust particles of a very narrow size distribution. From the thermoemission variations of this comet versus heliocentric distance Shulman (1974) concluded that the dust grains were semiconductive.

Jambor (1974) pointed out that there might be problems in reconciling existing models of the zodiacal cloud with the mechanism of dust contribution from short-period comets, in terms of both the amount of dust that can be supplied and particle sizes.

Delsemme (1973) discussed the general properties of cometary dust and assessed its role in maintaining the interplanetary cloud of dust in equilibrium. Vanýsek (1973) summarized the current state of knowledge on the composition of cometary dust, based on spectrophotometric, polarimetric and thermoemission measurements. Sekanina (1974c) reviewed the recent progress in the study of dust tails of comets and pointed to the most important directions for future research in the field, including the problem of evaporation and fragmentation of dust particles in the tail.

References

Benvenuti, P. (1974). Dust emission structure in comets with type II tails. Astrophys. Space Sci. 27, 203-209. [Ref. 11.102.004]

Bücher, A., Robley, R., and Koutchmy, S. (1975). Photometric, colorimetric and polarimetric study of Comet Kohoutek 1973f, on January 17 and 18, 1974. Astron. Astrophys. 39, 289-293.

Delsemme, A. H. (1973). Gas and dust in comets. Space Sci. Rev. 15, 89-101. [Ref. 10.102.011]

Gary, G. A., and O'Dell, C. R. (1974). Interpretation of the anti-tail of Comet Kohoutek as a particle flow phenomenon. Icarus 23, 519-525. [Ref. 12.103.104]

Gatley, I., Becklin, E. E., Neugebauer, G., and Werner, M. W. (1974). Infrared observations of Comet Kohoutek (1973f). Icarus 23, 561-565. [Ref. 12.103.104]

Gibson, E. G. (1974a). Comet Kohoutek drawings from Skylab. Sky and Tel. 48, 208-212. [Ref. 12.103.104]

Gibson, E. G. (1974b). Visual observations of Comet Kohoutek from Skylab III. Icarus 23, 493-501. [Ref. 12.103.104]

Grün, E., Hoffmann, H.-J., and Kissel, J. (1975). Dust emission from Comet Kohoutek (1973f) at large distances from the sun. (Abstract.) In Interplanetary Dust and Zodiacal Light, IAU Colloq. No. 31 (to be published).

Hoffmann, H.-J., Fechtig, H., Grün, E., and Kissel, J. (1974). Particles from Comet Kohoutek detected by the micrometeoroid experiment on HEOS 2. In The Study of Comets, IAU Colloq. No. 25 (in press).

Jambor, B. J. (1973). The split tail of Comet Seki-Lines. Astrophys. J. 185, 727-734. [Ref. 10.103.109]

Jambor, B. J. (1974). History of the dust released by comets. In The Study of Comets, IAU Colloq. No. 25 (in press).

Lamy, Ph. L., and Koutchmy, S. (1975). Study of the anti-tail of Comet Kohoutek from an observation on 17 January 1974. (Abstract.) In Interplanetary Dust and Zodiacal Light, IAU Colloq. No. 31 (to be published).

MacQueen, R. M. et al. (1974). Skylab white light coronograph photography. Presented at Comet Kohoutek Workshop, Marshall Space Flight Center, June 1974.

Ney, E. P. (1974a). Infrared observations of Comet Kohoutek near perihelion. Astrophys. J. (Lett.) 189, L141-L143. [Ref. 11.103.101]

Ney, E. P. (1974b). Multiband photometry of Comets Kohoutek, Bennett, Bradfield and Encke. Icarus 23, 551-560. [Ref. 12.103.007]

O'Dell, C. R. (1974). Particle sizes in Comet Bennett (1970 II). Icarus 21, 96-99. [Ref. 11.103.100]

Patashnick, H., and Rupprecht, G. (1975). The size dependence of sublimation rates for interplanetary ice particles. Astrophys. J. (Lett.) 197, L79-L82.

Rieke, G. H., and Lee, T. A. (1974). Photometry of Comet Kohoutek (1973f). Nature 248, 737-740. [Ref. 11.103.101]

Rieke, G. H., Low, F. J., Lee, T. A., and Wisniewski, W. (1974). Infrared observations of Comet Kohoutek. Presented at Comet Kohoutek Workshop, Marshall Space Flight Center, June 1974.

Sekanina, Z. (1973a). Dynamical and photometric investigation of cometary type II tails. NASA Grant NGR 09-015-159, Semiannual Progress Report No. 4, pp. 41-47. See also note in IAU Circ. No. 2580. [Ref. 10.103.102]

Sekanina, Z. (1973b). Existence of icy comet tails at large distances from the sun. Astrophys. Lett. 14, 175-180. [Ref. 10.102.005]

Sekanina, Z. (1974a). The prediction of anomalous tails of comets. Sky and Tel. 47, 374-377. [Ref. 11.102.021]

Sekanina, Z. (1974b). On the nature of the anti-tail of Comet Kohoutek (1973f). I. A working model. Icarus 23, 502-518. [Ref. 12.103.104]

Sekanina, Z. (1974c). Progress in our understanding of cometary dust tails. In The Study of Comets, IAU Colloq. No. 25 (in press).

Sekanina, Z. (1975a). A study of the icy tails of the distant comets. Icarus 25, 218-238.

Sekanina, Z. (1975b). Predicted favorable visibility conditions for anomalous tails of comets. In Interplanetary Dust and Zodiacal Light, IAU Colloq. No. 31 (to be published).

Sekanina, Z., and Miller, F. D. (1973). Comet Bennett 1970 II. Science 179, 565-567. [Ref. 09.103.102]

Sekanina, Z., and Miller, F. D. (1975). On the nature of the anti-tail of Comet Kohoutek (1973f). II. Comparison of the working model with ground-based photographic observations. Icarus (in press).

Shulman, L. M. (1974). Diagnostics of cometary dust from its infrared emission. Astrom. Astrophys. (Kiev) No. 23, 57-68. (In Russian.) [Ref. 12.102.012]

Spinrad, H., and Smith, H. E. (1973). Scans of Comet Bennett, 1969i. Icarus 19, 419-424. [Ref. 10.103.100]

Vanýsek, V. (1973). The composition of cosmic dust in comets. Space Res. XIII, Vol. 2, 1173-1179. [Ref. 12.102.013]

Weinberg, J. L., and Beeson, D. E. (1975). Photoelectric polarimetry of the tail of Comet Ikeya-Seki (1965 VIII). In The Study of Comets, IAU Colloq. No. 25 (in press).

Wurm, K. (1974). The substructure in the heads of comets with type I and type II tails. Astrophys. Space Sci. 27, 211-216. [Ref. 11. 102.105]